

On the deformation of a shear thinning viscoelastic drop in a steady electric field

Sarika Shivaji Bangar¹, Gaurav Tomar¹

Department of Mechanical Engineering, Indian Institute of Science, , Bengaluru, 560012, Karnataka, India

Abstract

The deformation of viscoelastic drops under electric fields plays a crucial role in applications such as microfluidics, inkjet printing, and electrohydrodynamic manipulation of complex fluids. This study examines the deformation and breakup dynamics of a linear Phan-Thien–Tanner (LPTT) drop subjected to a uniform electric field using numerical simulations performed with the open-source solver Basilisk. Representative combinations of conductivity ratio (σ_r) and permittivity ratio (ϵ_r) are chosen from six characteristic regions of the (σ_r, ϵ_r) phase space, PR_A^+ , PR_B^+ , PR_A^- , PR_B^- , OB^+ , and OB^- . In regions where the first- and second-order deformation coefficients have the same sign (PR_A^- , PR_B^- , OB^+), the LPTT drops exhibit deformation dynamics that negligibly deviate from the Newtonian behavior. In the PR_A^+ region, drops deform into prolate spheroidal shapes below a critical electric capillary number and transition to stable multi-lobed shapes or breakup beyond this threshold. Increasing elasticity of drop opposes the deformation, thereby reducing deformation and increasing critical Ca_E with the Deborah number (De). In the PR_B^+ region, drops form prolate shapes below critical Ca_E and develop conical ends above it. The steady-state deformation exhibits a non-monotonic dependence on De , increasing at low De and decreasing at higher values. A similar non-monotonic variation is also observed in critical Ca_E . In the OB^- region, LPTT drops attain oblate shapes below critical Ca_E and undergo breakup beyond it. The deformation magnitude shows a non-monotonic variation with De , increasing initially and decreasing at higher elasticity. Overall, these findings highlight the complex interplay between viscoelasticity and electric stresses in determining drop deformation, stability and morphology, offering insights for controlled manipulation of viscoelastic drops in electrohydrodynamic systems.

Keywords: linear PTT, drops, viscoelasticity, electric-field, finite extensibility

1. Introduction

Understanding the deformation dynamics of droplets in electric fields is fundamental to a wide range of applications, including inkjet printing (Basaran et al. (2013), Lau and Shrestha (2017)), oil de-emulsification (Eow and Ghadiri (2002), Alvarado and Manrique (2010), Zhang et al. (2011)), electrospraying and atomization (Kelly

(1984), Law (2018)), electrostatic coating (Hines (1966)), electric propulsion (Moreau et al. (2015), Huh and Wirz (2019)), and droplet manipulation in microfluidics (Laser and Santiago (2004), Stone et al. (2004), Phan et al. (2025)). These processes also shed light on natural phenomena such as rain electrification and droplet breakup in thunderstorms (Simpson (1909), Wilson (1921), Blanchard (1963)).

A dielectric drop subjected to an electric field typically elongates into a prolate spheroid at low field strengths and undergoes breakup at high fields (O’Konski and Thacher Jr (1953), Taylor (1964)). Allan and Mason (1962) attributed this deformation to the balance between interfacial electric stresses and surface tension, while O’Konski and Thacher Jr (1953) arrived at similar conclusions using an energy-based approach. To explain the experimentally observed oblate shapes, O’Konski and Harris (1957) identified fluid conductivity as a key parameter governing prolate and oblate forms. Building on these insights, Taylor (1966) developed the classical leaky-dielectric model (LDM), demonstrating that tangential electric stresses induce internal circulation and dictate the deformation mode based on conductivity and permittivity ratios. This framework was later refined by Melcher and Taylor (1969), extended to alternating fields by Torza et al. (1971), and further corrected for higher-order effects by Ajayi (1978). However, experimental observations by Torza et al. (1971) revealed deformations larger than theoretical predictions, and higher-order corrections failed to reconcile this difference. Saville (1997) has provided a comprehensive review of the leaky dielectric model.

The LDM and its extensions have since been used to analyze diverse electrohydrodynamic (EHD) phenomena. Surfactants were shown to amplify deformation, particularly for prolate shapes (Ha and Yang (1995)), while the extended LDM (ELDM) (Bentenitis and Krause (2005)) captured hysteresis and continuous deformation at high fields. Zabaranin (2013) modeled moderate deformations using a spheroidal approximation, while Nganguia et al. (2013) extended this to surfactant-laden drops. Deshmukh and Thakkar (2013) further showed that in quadrupole fields, deformation is dominated by the fourth-order Legendre mode with complex internal circulation. Drop electrorotation, first examined by He et al. (2013) and later generalized by Yariv and Frankel (2016), was linked to surface charge convection and Quincke-type instabilities. The Taylor–Melcher framework has since been applied to a wide range of symmetry-breaking instabilities, including Quincke rotation, equatorial streaming and pattern formation Vlahovska (2016), Vlahovska (2019). The charge convection is shown to strongly affect the breakup dynamics (Sengupta et al. (2017)).

Sozou (1972) first analyzed transient drop deformation by incorporating fluid inertia into the governing equations. Using a quasi-steady approximation, Moriya et al. (1986) studied time-dependent deformation in weak fields. Esmaeeli and Sharifi (2011) derived a closed-form solution quantifying the roles of normal and tangential electric stresses. Zhang et al. (2013) extended the Taylor–Melcher model to include finite charge relaxation time for spheroidal drops. Lanauze et al. (2013) further accounted for inertia and showed that deformation overshoot depends on the Ohnesorge and Saville numbers. Lanauze et al. (2015) examined nonlinear effects with surface charge convection, revealing transient prolate-to-oblate transitions. Esmaeeli and

Behjatian (2020) performed 3D simulations showing that drop dynamics range from monotonic to oscillatory depending on viscous–inertial timescales.

Experimental efforts have provided further insights into EHD deformation and breakup. Nishiwaki et al. (1988) experimentally related drop retardation time to fluid properties, finding good agreement with theory for viscous drops but lower deformation for water. Vizika and Saville (1992) observed improved, though not perfect, consistency with leaky-dielectric predictions under steady and oscillatory fields. Karp et al. (2024) used PIV and shadowgraphy to show close agreement with the model for small deformations. Brosseau and Vlahovska (2017) reported equatorial streaming in low-viscosity drops under strong DC fields, driven by electric shear stresses that concentrate flow and trigger fluid ejection at the equator.

Numerical studies have significantly advanced the understanding of Newtonian EHD behavior. Miksis (1981) used boundary integrals to show that dielectric drops form conical ends above a critical permittivity ratio, while Sherwood (1988) extended this to leaky-dielectric drops, predicting breakup modes such as tip streaming and blob formation. His results linked high permittivity ratios to pointed-end drops and high conductivities to blob division, though the analysis was limited to prolate deformations. Feng and Scott (1996) solved the full EHD problem via finite element method, identifying a critical electric field for instability and showing strong dependence on conductivity and viscosity ratios; Feng (1999) later found charge convection reduces oblate but enhances prolate deformation. Lac and Homsy (2007) analyzed stability across wide property ratios, including oblate modes. Dubash and Mestel (2007) captured steady and breakup regimes for inviscid conducting drops, while Karyappa et al. (2014) classified viscosity-dependent breakup identifying three axisymmetric prior to breakup (ASPB) modes (lobes, pointed, non-pointed ends) that transform into non-axisymmetric shape at breakup (NSAB) modes (charged disintegration, regular jet, open jet). More recent studies by Wagoner et al. (2021) and Wang et al. (2024), linked equatorial streaming and fingering instabilities to coupled surface charge convection and diffusion under strong DC fields.

Several computational techniques have been developed for simulating multiphase EHD flows. Zhang and Kwok (2005) introduced a 2D multicomponent LBM, while Tomar et al. (2007) used a coupled level-set/VOF method and proposed weighted harmonic mean interpolation for property smoothing. Hua et al. (2008) combined front-tracking and VOF methods for various electric models, and Paknemat et al. (2012) used a level-set method with a finite difference based ghost fluid approach to capture tip-streaming and breakup. Nganguia et al. (2015) employed the Immersed Interface Method, and Das and Saintillan (2017) developed a 3D boundary element method including surface charge convection and Quinke rotation. Later, Liu et al. (2019) and Wang et al. (2024) advanced LBM-based multiphase solvers coupling Allen–Cahn, Poisson, and Navier–Stokes equations for charge and field evolution.

Many natural and industrial fluids, such as polymer solutions and biological fluids, are viscoelastic, exhibiting coupled viscous and elastic responses that lead to normal stress differences, stress relaxation, and strain hardening. These effects alter interfacial dynamics, delaying breakup and modifying the critical capillary number.

Ramaswamy and Leal (1999), Hooper et al. (2001), and Aggarwal and Sarkar (2007) showed that viscoelasticity generally reduces drop deformation, enhances shape recovery, and increases breakup resistance in extensional and shear flows. Despite the prevalence of viscoelastic drops in numerous natural and industrial systems, literature on their electrohydrodynamics is limited. Ha and Yang (1999) investigated the effect of viscoelasticity on drop deformation and stability in an electric field using a second-order fluid model. Building on this, Ha and Yang (2000) analyzed Newtonian and non-Newtonian conducting drops, showing that both shear-independent and shear-rate-dependent viscoelastic fluids exhibit reduced deformation and improved stability. They further found that elasticity in the surrounding phase stabilizes drops at low viscosity ratios but can induce instability at higher ratios. Later, Lima and d’Avila (2014) numerically studied a Giesekus drop and showed that increasing polymer relaxation time suppresses deformation through elastic resistance while also lowering effective viscosity via shear thinning. More recently, Zhao et al. (2025) examined viscoelastic drops in combined electric and shear flows, finding that elasticity diminishes deformation and rotation, though its impact remains secondary to electrohydrodynamic stresses. Recently, Das et al. (2026) developed an analytical approximation for the deformation of an Oldroyd-B drop in an electric field in the small Deborah number regime and conducted numerical simulations to study the drop dynamics at higher Deborah numbers. In a recent study, Bangar and Tomar (2026) investigated the large deformation of an Oldroyd-B drop subjected to an electric field. Although the Oldroyd-B model captures the elastic nature of viscoelastic fluids, it does not account for shear-thinning behavior and permits infinite extension of polymer molecules, which is physically unrealistic.

Motivated by these limitations, the present study investigates the deformation of a drop described by the linear Phan-Thien–Tanner (LPTT) model subjected to a steady uniform electric field. The LPTT model incorporates finite polymer extensibility and shear-thinning behavior, providing a more realistic representation of viscoelastic fluid behavior. Pairs of conductivity (σ_r) and permittivity (ϵ_r) ratios are selected based on the deformation–circulation phase map (Lac and Homsy (2007), Bangar and Tomar (2026)) obtained from small-deformation analysis (Das et al. (2026)). The governing equations and boundary conditions are described in §2, followed by the numerical methodology and grid independence study in §3. The results are discussed in §4, and the key conclusions of the study are summarized in §5.

2. Problem Formulation

A viscoelastic drop of radius R , suspended in a Newtonian fluid, is subjected to a uniform, steady electric field E_∞ . Subscripts i and e denote the drop and ambient phases, respectively. Each phase is characterized by its density ρ , viscosity μ , permittivity ϵ , and conductivity σ . The ambient fluid is Newtonian, while the drop is modeled using the linear Phan–Thien–Tanner (PTT) constitutive equation with relaxation time λ_i , solvent and polymeric viscosities μ_{i_s} and μ_{i_p} , and extensibility

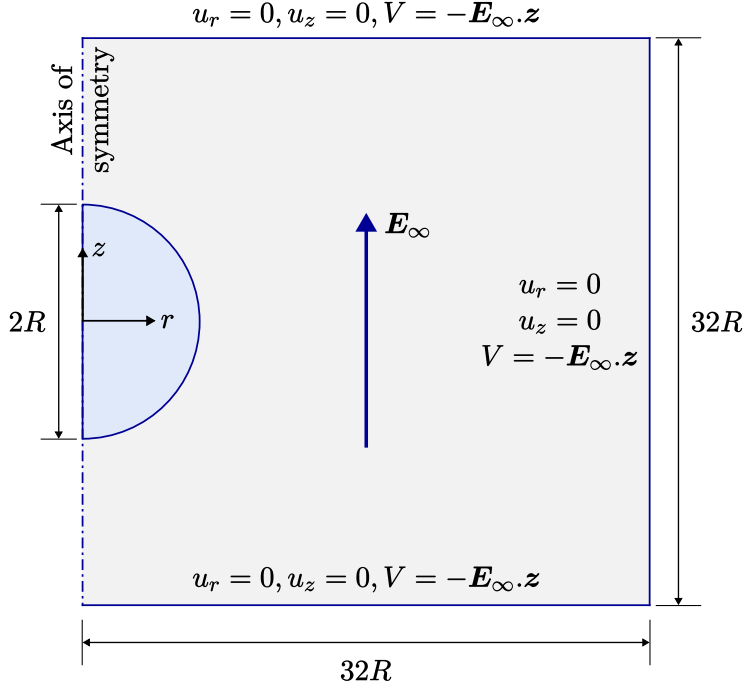


Figure 1: Schematic of the problem. LPTT drop of radius R is subjected to an external electric field, \mathbf{E}_∞ , aligned along the axis of symmetry. The domain size is set to $32R \times 32R$ to minimize the boundary effects.

parameter ε . Axisymmetric simulations are performed using the open-source solver [Basilisk](#) (Popinet (2015)), and the system schematic is shown in [Figure 1](#).

2.1. Governing Equations

The incompressible fluid flow is governed by the mass and momentum conservation equations:

$$\nabla \cdot \mathbf{u} = 0, \quad \rho \frac{D\mathbf{u}}{Dt} = -\nabla p + \nabla \cdot \boldsymbol{\tau} + \mathbf{F}, \quad (1)$$

where \mathbf{u} is the velocity, ρ the density, p the pressure, $\boldsymbol{\tau}$ the stress tensor, and \mathbf{F} the body force. The stress tensor is related to the velocity gradient through a constitutive relation. In the presence of an electric field \mathbf{E} , the body force arises from the Maxwell stress tensor $\boldsymbol{\tau}_E$ as

$$\mathbf{F} = \nabla \cdot \boldsymbol{\tau}_E, \quad \boldsymbol{\tau}_E = \epsilon \left(\mathbf{E}\mathbf{E} - \frac{1}{2}(\mathbf{E} \cdot \mathbf{E})\mathbf{I} \right), \quad (2)$$

where ϵ is the permittivity.

The viscoelastic drop is modeled using the linear Phan–Thien–Tanner (LPTT) model, where the total stress is

$$\boldsymbol{\tau} = \boldsymbol{\tau}_s + \boldsymbol{\tau}_p, \quad (3)$$

with the solvent stress $\boldsymbol{\tau}_s = 2\mu_s \boldsymbol{D}$, where $\boldsymbol{D} = \frac{1}{2}(\nabla \boldsymbol{u} + (\nabla \boldsymbol{u})^T)$, and the polymeric stress tensor evolves according to

$$\boldsymbol{\tau}_p \left(1 + \frac{\varepsilon \lambda}{\mu_p} \text{tr}(\boldsymbol{\tau}_p) \right) + \lambda \overset{\nabla}{\boldsymbol{\tau}}_p = \mu_p (\nabla \boldsymbol{u} + (\nabla \boldsymbol{u})^T), \quad (4)$$

where λ is the relaxation time, $\mu_p = \mu - \mu_s$ the polymeric viscosity, ε the extensibility parameter, and $\overset{\nabla}{\boldsymbol{\tau}}_p$ denotes the upper-convected derivative.

Magnetic effects are neglected as the characteristic magnetic time $t_M = \mu_M \sigma L^2$ is much smaller than the electric relaxation time $t_E = \varepsilon / \sigma$. The electric field is governed by Gauss's and Faraday's laws:

$$\nabla \cdot (\varepsilon \boldsymbol{E}) = q, \quad \nabla \times \boldsymbol{E} = 0, \quad (5)$$

where, q denotes the volumetric charge density. Electric field can be represented in terms of a gradient of electric potential ($\boldsymbol{E} = -\nabla V$), leading to the following equation for the electric potential,

$$\nabla \cdot (\varepsilon \nabla V) = -q. \quad (6)$$

The bulk free charge conservation is expressed as

$$\frac{\partial q}{\partial t} + \nabla \cdot \boldsymbol{J} = 0, \quad \boldsymbol{J} = \sigma \boldsymbol{E} + q \boldsymbol{u}, \quad (7)$$

where the first term in \boldsymbol{J} represents Ohmic conduction and the second term represents charge convection. Solving these equations numerically provides the electric field distribution, which is used to compute $\boldsymbol{\tau}_E$ and the resulting electric body force.

2.2. Boundary Conditions

A schematic of the simulation domain is shown in [Figure 1](#), with the origin of the (r, z) coordinate system at the drop center. The domain extends from $-L/2$ to $L/2$ in z and from 0 to L in r . Far from the drop, the velocity vanishes:

$$u_r(r, -L/2) = u_z(r, -L/2) = 0 \quad (8a)$$

$$u_r(r, L/2) = u_z(r, L/2) = 0, \quad (8b)$$

$$u_r(L, z) = u_z(L, z) = 0. \quad (8c)$$

The imposed uniform electric field \boldsymbol{E}_∞ is represented by the potential V :

$$\boldsymbol{E}_\infty = -\nabla V, \quad V = -E_\infty z. \quad (9)$$

Accordingly, the electric potential satisfies

$$V(r, -L/2) = V(r, L/2) = V(L, z) = -E_\infty z. \quad (10a)$$

All polymeric stress components are assigned Neumann boundary conditions far from the drop, which introduces only local errors (Alves et al. (2021)). Symmetry is imposed at the axis $r = 0$:

$$u_r(0, z) = 0, \quad \frac{\partial u_z}{\partial r} \Big|_{r=0} = 0 \quad (11a)$$

$$\frac{\partial V}{\partial r} \Big|_{r=0} = 0, \quad (11b)$$

$$\frac{\partial \tau_{prr}}{\partial r} \Big|_{r=0} = \frac{\partial \tau_{pzz}}{\partial r} \Big|_{r=0} = \tau_{prz}(0, z) = \frac{\partial \tau_{p\theta\theta}}{\partial r} \Big|_{r=0} = 0. \quad (11c)$$

2.3. Non-dimensional Parameters

To simplify the analysis, we non-dimensionalize the governing equations. The drop radius R is used as a characteristic length scale and the magnitude of the imposed electric field, E_∞ is taken as a characteristic scale for the electric field. The velocity scale is obtained by the balance of electric and viscous stress,

$$U \sim \frac{\epsilon_e E_\infty^2 R}{\mu_e}. \quad (12)$$

As flow is viscous dominated, stresses and pressure are non-dimensionalized by the viscous scale, $\mu_e U/R$. This viscous stress scale is equivalent to the electric stress scale $\epsilon_e E_\infty^2$, as the velocity scale itself is derived from their balance. Upon non-dimensionalization of the governing equations, we get the following dimensionless parameters that affect the problem:

1. Permittivity ratio, $\epsilon_r = \frac{\epsilon_i}{\epsilon_e}$
2. Conductivity ratio, $\sigma_r = \frac{\sigma_i}{\sigma_e}$
3. Density ratio, $\rho_r = \frac{\rho_i}{\rho_e}$
4. Viscosity ratio, $\mu_r = \frac{\mu_i}{\mu_e}$
5. Flow Reynolds number, $Re = \frac{\rho_e U R}{\mu_e}$
6. Electric capillary number, $Ca_E = \frac{\epsilon_e E_\infty^2 R}{\gamma}$, is the ratio of electric force to surface tension force with the surface tension being a resisting force and the force due to the electric field being a deforming force.
7. Deborah number, $De = \frac{\lambda_i U}{R}$, is the ratio of the polymer relaxation time to the flow time scale.
8. Ratio of solvent to total viscosity of the drop phase, $\beta_i = \frac{\mu_{is}}{\mu_i}$
9. Extensibility parameter of LPTT fluid, ε

3. Numerical Simulations

3.1. Numerical Methodology

For the axisymmetric numerical simulations, we employ the open-source solver [Basilisk](#) (Popinet (2015)), which simulates two-phase flows using a geometric Volume

of Fluid (VOF) method. The solver uses a second-order accurate time-splitting projection scheme with variables stored at cell centers. Diffusion terms are treated implicitly, while advection is discretized using the second-order Bell-Collela-Glaz (BCG) scheme. Equation for electric potential and charge conservation equation are solved by the numerical scheme given in [López-Herrera et al. \(2011\)](#). The viscoelastic constitutive equation is solved using the log-conformation tensor approach as described by [Fattal and Kupferman \(2004\)](#). The polymeric stress is expressed in terms of a symmetric positive definite tensor \mathbf{A} as $\boldsymbol{\tau}_p = \frac{\mu_p}{\lambda}(\mathbf{A} - \mathbf{I})$. Introducing $\boldsymbol{\Psi} = \log \mathbf{A}$, its evolution equations is written as:

$$\frac{\partial \boldsymbol{\Psi}}{\partial t} + \underbrace{\mathbf{u} \cdot \nabla \boldsymbol{\Psi}}_{\text{Advection}} = \underbrace{\boldsymbol{\Omega} \boldsymbol{\Psi} - \boldsymbol{\Psi} \boldsymbol{\Omega} + 2\mathbf{B}}_{\text{Upper convection}} + \underbrace{\frac{1}{\lambda} \left(1 + \frac{\varepsilon \mu_p}{\lambda} (\text{Tr}(e^{\boldsymbol{\Psi}}) - 3) \right)}_{\text{Model term}} (e^{-\boldsymbol{\Psi}} - \mathbf{I}). \quad (13)$$

The evolution equation for $\boldsymbol{\Psi}$ is solved using a split scheme given by [López-Herrera et al. \(2019\)](#).

$$\frac{\partial \boldsymbol{\Psi}}{\partial t} = \boldsymbol{\Omega} \boldsymbol{\Psi} - \boldsymbol{\Psi} \boldsymbol{\Omega} + 2\mathbf{B} \quad (14)$$

$$\frac{\partial \boldsymbol{\Psi}}{\partial t} + \nabla \cdot (\mathbf{u} \boldsymbol{\Psi}) = 0 \quad (15)$$

$$\frac{\partial \mathbf{A}}{\partial t} = \frac{1}{\lambda} (\mathbf{I} - \mathbf{A}) \left(1 + \frac{\varepsilon \mu_p}{\lambda} \text{Tr}(\mathbf{A} - \mathbf{I}) \right) \quad (16)$$

The upper-convected derivative ([Equation 14](#)) is computed explicitly, advection of $\boldsymbol{\Psi}$ ([Equation 15](#)) is handled using the BCG scheme, and the LPTT model term ([Equation 16](#)) is integrated implicitly via the Euler method.

Table 1: Coordinates of the primary eddy center and minimum horizontal velocity along $x = 0.5$ line and location of its occurrence for lid driven cavity flow of LPTT fluid

LPTT	Re	De	β	ε	x_{eddy}	y_{eddy}	u_{min}	y_{min}
Dalal et al. (2016)	1	1	0.3	0.25	0.481	0.789	-0.1679	0.5349
Present					0.483	0.789	-0.1676	0.533
Dalal et al. (2016)	1	1	1/9	0.1	0.453	0.800	-0.1416	0.5116
Present					0.460	0.804	-0.1393	0.514
Dalal et al. (2016)	100	1	1/9	0.25	0.778	0.845	-0.1037	0.5387
Present					0.781	0.851	-0.1026	0.541
Dalal et al. (2016)	100	4	1/9	0.25	0.783	0.767	-0.0858	0.3363
Present					0.789	0.781	-0.0844	0.338

To validate the implementation, simulations of lid-driven cavity flow for an LPTT fluid are performed across a range of parameters. The results are compared with the numerical findings of [Dalal et al. \(2016\)](#). [Table 1](#) presents a comparison of the primary eddy position and the minimum horizontal velocity along the $x = 0.5$ centerline, including its location, while [Table 2](#) lists the minimum and maximum vertical

Table 2: Minimum and maximum values of vertical velocity along the $y = 0.5$ line and position of their occurrence for lid driven cavity flow of LPTT fluid

LPTT	Re	De	β	ε	v_{min}	x_{min}	v_{max}	x_{max}
Dalal et al. (2016)	1	1	0.3	0.25	-0.1429	0.7950	0.1572	0.2016
Present	1	1	0.3	0.25	-0.1426	0.795	0.1568	0.201
Dalal et al. (2016)	1	1	1/9	0.1	-0.1235	0.7883	0.1484	0.1883
Present	1	1	1/9	0.1	-0.1213	0.787	0.1454	0.189
Dalal et al. (2016)	100	1	1/9	0.25	-0.1050	0.8559	0.0753	0.2339
Present	100	1	1/9	0.25	-0.1021	0.853	0.0742	0.233
Dalal et al. (2016)	100	4	1/9	0.25	-0.1301	0.9059	0.0903	0.2489
Present	100	4	1/9	0.25	-0.1265	0.904	0.0887	0.248

velocities along the $y = 0.5$ centerline with their respective locations. The tabulated results demonstrate good agreement with the literature, confirming the accuracy and robustness of the numerical approach.

3.2. Grid convergence and domain independence study

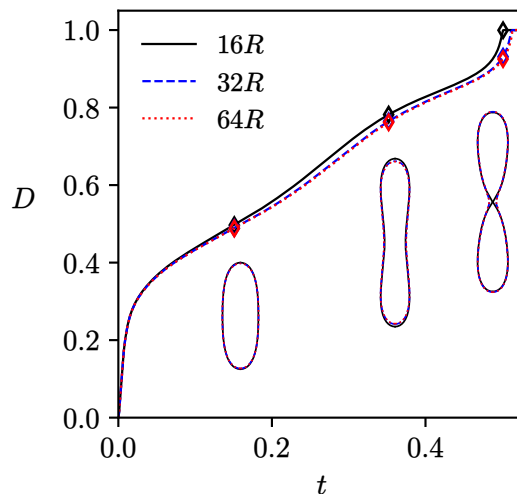


Figure 2: Deformation vs. time for various sizes of the simulation domain. Simulation parameters are $\mu_r = 1$, $\rho_r = 1$, $Re = 1$, $\beta_i = 1/9$, $\sigma_r = 10$, $\epsilon_r = 1.37$, $De = 5$, $Ca_E = 0.4$, $\varepsilon = 0.25$. $R/\Delta x_{min}$ is taken as 256.

A domain independence test is conducted to determine the appropriate simulation domain size, as illustrated in Figure 2. Numerical simulations are performed using three different domain sizes, and the evolution of the drop deformation parameter over time is examined. The figure also presents the interface shapes at three distinct time instances for each domain size. Results show that the deformation behavior

for domains of size $32R$ and $64R$ closely overlap, indicating negligible difference. Consequently, a domain size of $32R$ is selected for all subsequent simulations in this study.

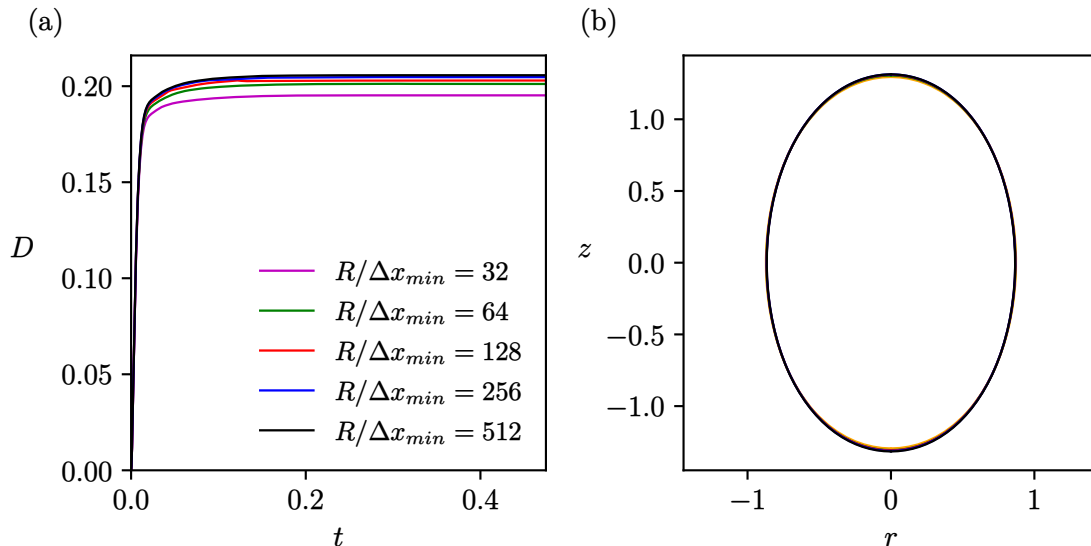


Figure 3: (a) Deformation parameter variation with time at various refinements of the grid. (b) Steady state deformed interface of the drop for various grid refinements. Simulation parameters: $Re = 1$, $Ca_E = 0.4$, $De = 5$, $\sigma_r = 10$, $\epsilon_r = 1.37$, $\beta = 1/9$, $\epsilon = 0.25$

Further, a grid independence study is performed to ensure that the simulation results are not dependent on the grid resolution. We use the adaptive mesh refinement for the numerical simulations and grid refinement is characterized by the parameter $R/\Delta x_{min}$. Figure 3 shows the grid convergence study. Figure 3(a) shows the variation of deformation parameter with time for different grid refinements. We can see that results for $R/\Delta x_{min} = 512$ and $R/\Delta x_{min} = 256$ are almost overlapping with each other. Figure 3(b) shows the steady state interface shape for various grid refinements. The values of deformation parameter and the relative percentage error for various grid refinements are shown in Table 3. As relative percentage error for $R/\Delta x_{min} = 256$ is less than 1 percent, we have considered $R/\Delta x_{min} = 256$ for conducting the numerical simulations in this study.

4. Results and discussion

The drop deformation is characterized using Taylor's deformation parameter,

$$D = \frac{L - B}{L + B} \quad (17)$$

where L and B denote the drop dimensions along and perpendicular to the applied electric field, respectively.

Table 3: The deformation parameter and relative percentage error for different grid refinements

$R/\Delta x_{min}$	D	$e_{rel} = \frac{ D-D_{512} }{ D_{512} } \times 100$
32	0.19522819	5.092270099
64	0.20115761	2.209757118
128	0.20295425	1.336343172
256	0.20471908	0.478393257
512	0.20570315	0

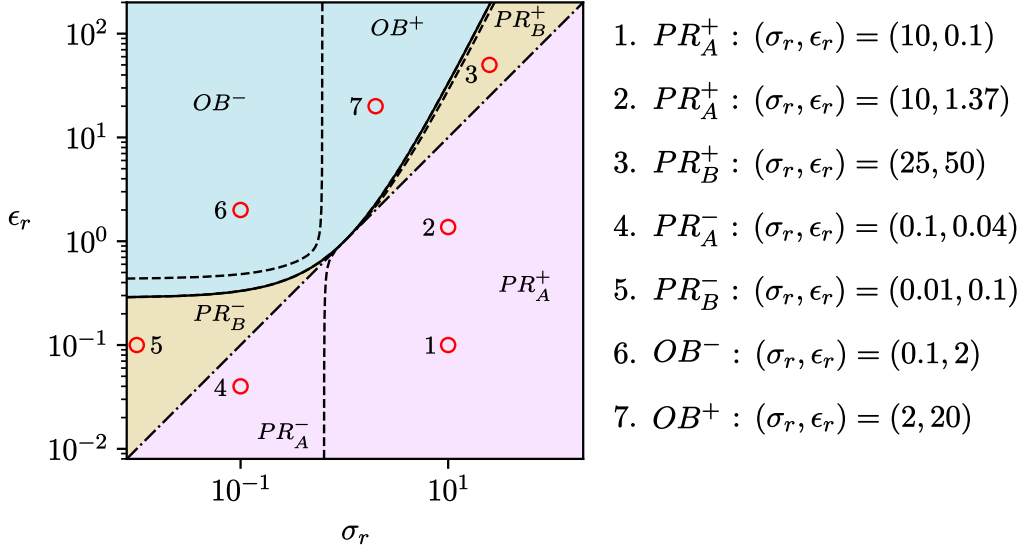


Figure 4: (σ_r, ϵ_r) pairs selected for the study are enumerated and marked (red circle markers) on (σ_r, ϵ_r) phase plot on log-log scale.

In this study, the electrohydrodynamic deformation of a viscoelastic drop is investigated for $\rho_r = 1$, $\mu_r = 1$, $Re = 1$, $\epsilon = 0.25$, and $\beta_i = 1/9$. Six distinct regions on the (σ_r, ϵ_r) plane, denoted PR_A^+ , PR_B^+ , PR_A^- , PR_B^- , OB^- , and OB^+ , identified from asymptotic analysis (Bangar and Tomar (2026)), serve as the basis for the selection of conductivity ratio and permittivity ratio for the study. Two points from PR_A^+ and a representative point from each of the other regions, are selected for the study. Selected points are enumerated and marked on (σ_r, ϵ_r) plot, are shown in Figure 4. For each selected pair, numerical simulations are performed over a range of Ca_E and De . The dimensional parameters are fixed as: drop radius $R = 0.001$, ambient density $\rho_e = 1000$, ambient permittivity $\epsilon_e = 4.425 \times 10^{-11}$, ambient conductivity $\sigma_e = 10^{-5}$, and interfacial tension $\gamma = 0.065$. Remaining dimensional parameters are obtained from the specified non-dimensional values. The velocity scale, obtained from the balance of electric and viscous stresses, is $U = 0.2549\sqrt{Ca_E}$ leading to an electric Reynolds number $Re_E = \frac{\epsilon_e U}{R\sigma_e} = 1.128 \times 10^{-3}\sqrt{Ca_E}$.

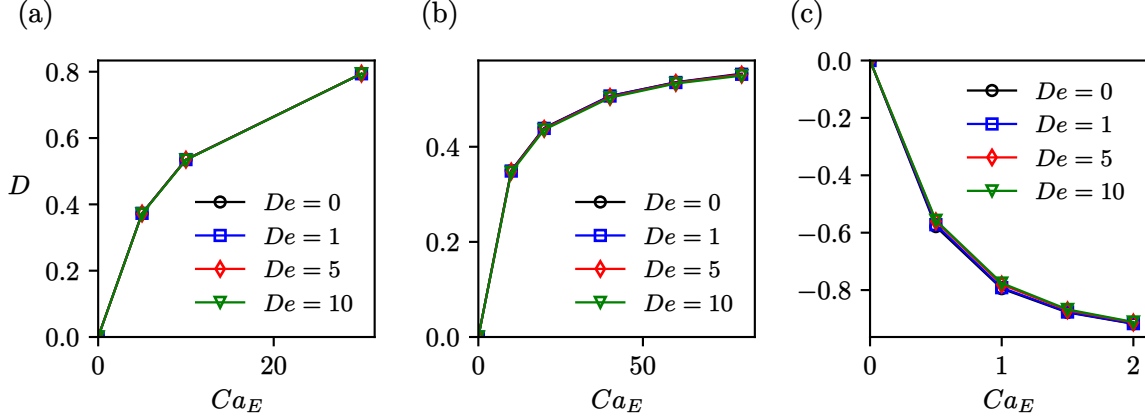


Figure 5: Deformation versus Ca_E for various De , for $\rho_r = 1$, $\mu_r = 1$, $Re = 1$, $\beta_i = 1/9$, $\varepsilon = 0.25$. (a) $\sigma_r = 0.1$, $\varepsilon_r = 0.04$ (PR_A^-) (b) $\sigma_r = 0.01$, $\varepsilon_r = 0.1$ (PR_B^-) (c) $\sigma_r = 2$, $\varepsilon_r = 20$ (OB^+)

Building on the Newtonian drop analysis of [Lac and Homsy \(2007\)](#) ($De = 0$) and the analysis of Oldroyd B drop by [Bangar and Tomar \(2026\)](#), the present work extends the investigation to linear PTT drops subjected to steady electric fields. In the PR_A^- , PR_B^- , and OB^+ regions, the first and second order deformation coefficients have opposite signs, and stable drop shapes are attained even at large Ca_E . For these regions, [Figure 5](#) shows that the deviation from Newtonian behavior is negligible. Thus, for subsequent discussions, we focus on PR_A^+ , PR_B^+ and OB^- regions of $(\sigma_r, \varepsilon_r)$ plane.

4.1. The drop behavior for $(\sigma_r, \varepsilon_r)$ from PR_A^+

4.1.1. The drop behavior for $(\sigma_r, \varepsilon_r) = (10, 0.1)$

Similar to the Newtonian case, a viscoelastic drop with $(\sigma_r, \varepsilon_r) = (10, 0.1)$ in the PR_A^+ regime deforms into a stable prolate spheroid under the action of a uniform, steady electric field, provided the electric capillary number (Ca_E) remains below a critical threshold. Beyond this threshold, the drop undergoes breakup. [Figure 6](#) presents the time evolution of the drop interface for various combinations of Ca_E and Deborah number (De). For cases resulting in a stable spheroidal deformation, only the final equilibrium interface is plotted (blue). When a stable configuration is not attained, the interface at two intermediate times and at the terminal simulation time is shown (red). These snapshots are chosen to highlight the characteristic stages of deformation and breakup for each (Ca_E, De) pair. The figure reveals a distinct dependence of the breakup threshold on viscoelasticity. At higher Deborah numbers ($De \geq 5$), the drop retains a stable spheroidal shape for $Ca_E \leq 0.36$, but transitions to multi-lobed deformations and eventual breakup once $Ca_E \geq 0.37$, placing the critical capillary number Ca_E^{crit} in the range $(0.36, 0.37)$. In contrast, at lower Deborah numbers ($De \leq 1$), spheroidal stability persists only up to $Ca_E \leq 0.34$, while instability and breakup occur for $Ca_E \geq 0.35$, indicating $Ca_E^{crit} \in (0.34, 0.35)$. These results clearly demonstrate that the critical electric capillary number increases with

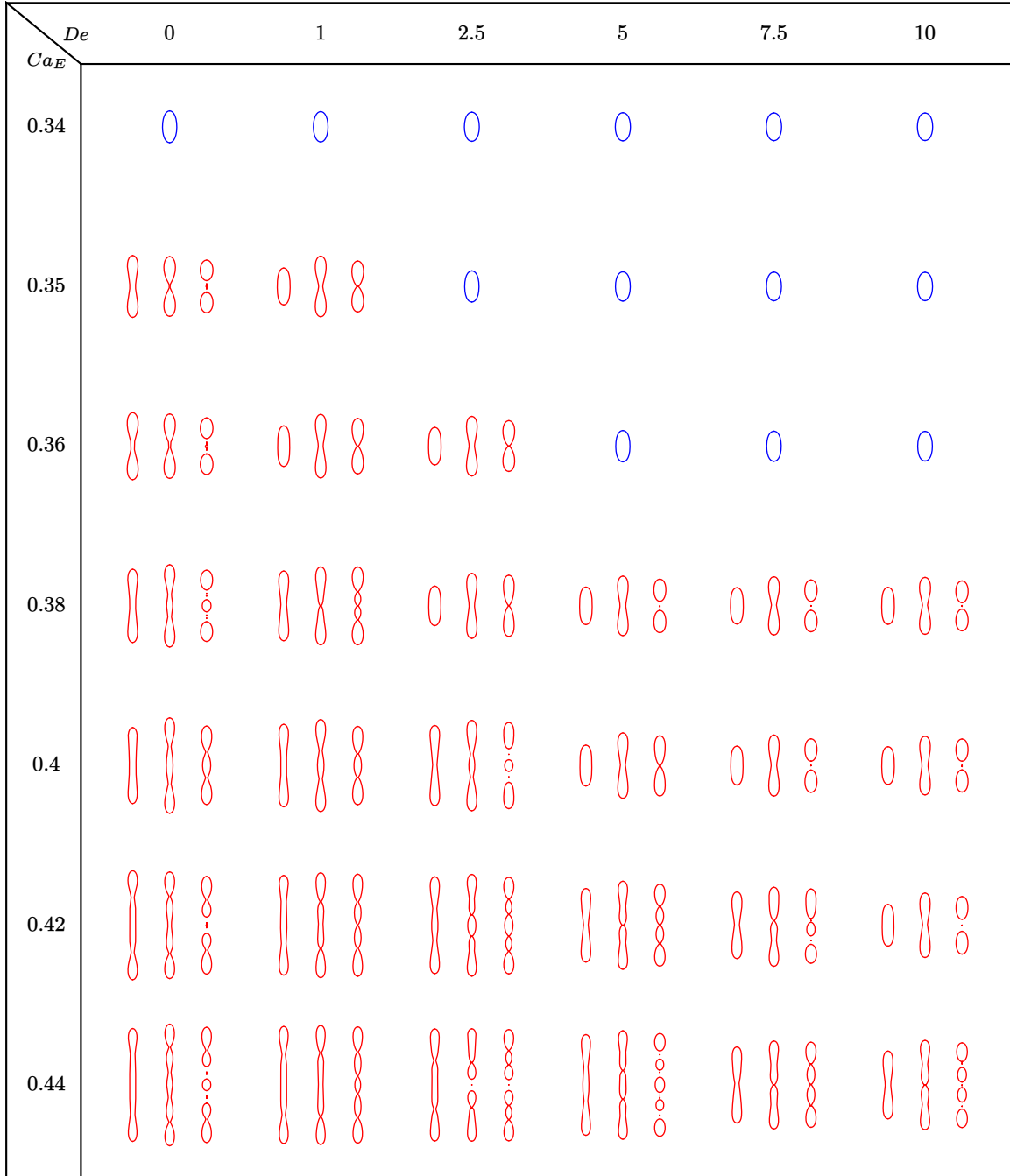


Figure 6: Behavior of drop interface in presence of electric field for various values of Ca_E and De for $(\sigma_r, \epsilon_r) = (10, 0.1)$, $\mu_r = 1$, $\rho_r = 1$, $Re = 1$, $\varepsilon = 0.25$, $\beta_i = 1/9$

increasing Deborah number, underscoring the stabilizing influence of viscoelasticity on drop deformation under electric fields.

Figure 7(a) illustrates the variation of stable spheroidal drop deformation with the electric capillary number (Ca_E) for $(\sigma_r, \epsilon_r) = (10, 0.1)$ at different Deborah numbers (De). Similar to Newtonian drops, the deformation curves exhibit a positive curvature

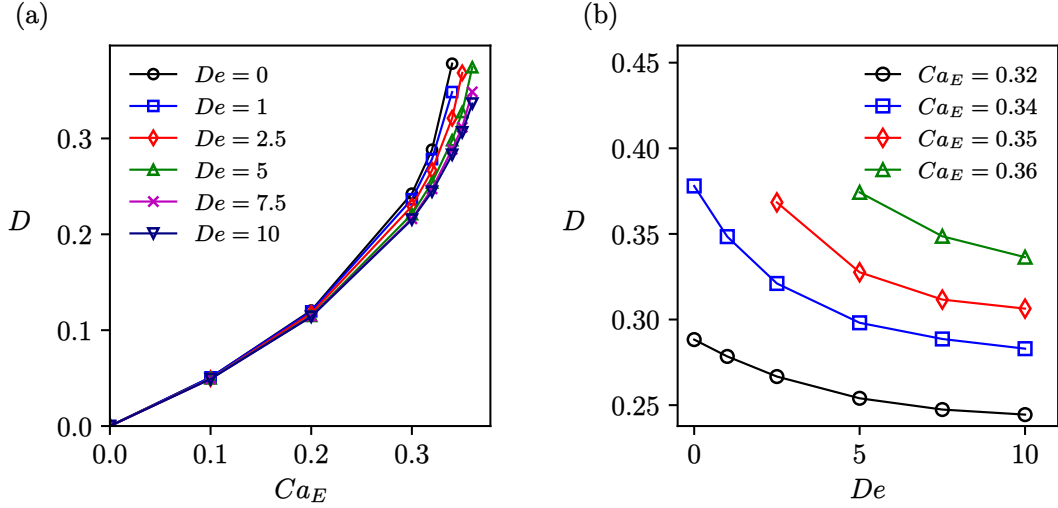


Figure 7: (a) Deformation versus Ca_E for various De , (b) Deformation versus De for various Ca_E , for $\rho_r = 1$, $\mu_r = 1$, $Re = 1$, $\sigma_r = 10$, $\epsilon_r = 0.1$, $\beta_i = 1/9$, $\varepsilon = 0.25$. (from PR_A^+)

across all De . However, for a fixed Ca_E , the extent of deformation decreases as De increases, highlighting the elastic resistance of the drop to deformation. This trend is further quantified in Figure 7(b), which depicts the dependence of deformation on De for various Ca_E . The results show a monotonic reduction in deformation with increasing De , followed by a saturation at higher Deborah numbers, indicating that beyond a certain elasticity, further increases in De exert a diminishing influence on drop deformation.

Figure 8 illustrates the temporal evolution of the drop interface at a constant electric capillary number ($Ca_E = 0.38$) across various Deborah numbers (De). At $Ca_E = 0.38$, the breakup morphology varies significantly with the Deborah number (De). For $De \geq 2.5$, the drop primarily undergoes a two-lobed breakup. Specifically, for $De = 5, 7.5$, and 10 , these lobes initially separate but then approach each other, while at $De = 2.5$, the two lobes remain attached (or immediately reattach upon breakup). When $De = 0$, a three-lobed breakup is observed. In contrast, at $De = 1$, an initial two-lobed breakup occurs, with each resulting lobe subsequently undergoing further breakup to yield a four-lobed structure. The temporal evolution of deformation parameter for various De values, up to the first breakup event, is also illustrated. A rapid increase in deformation precedes breakup, particularly for cases exhibiting two-lobed initial breakup. We note a trend, where, the initial number of breakup lobes decreases with increasing De : three lobes for $De = 0$, and two lobes for $De \geq 1$. As previously mentioned, for $De = 1$, these elongated initial lobes undergo secondary breakup, leading to a four-lobed final structure. Significantly, for $De \geq 2.5$, the breakup time increases with increasing De , indicating a delayed breakup for higher Deborah numbers.

Moving to a higher electric capillary number, $Ca_E = 0.44$, Figure 9 depicts the

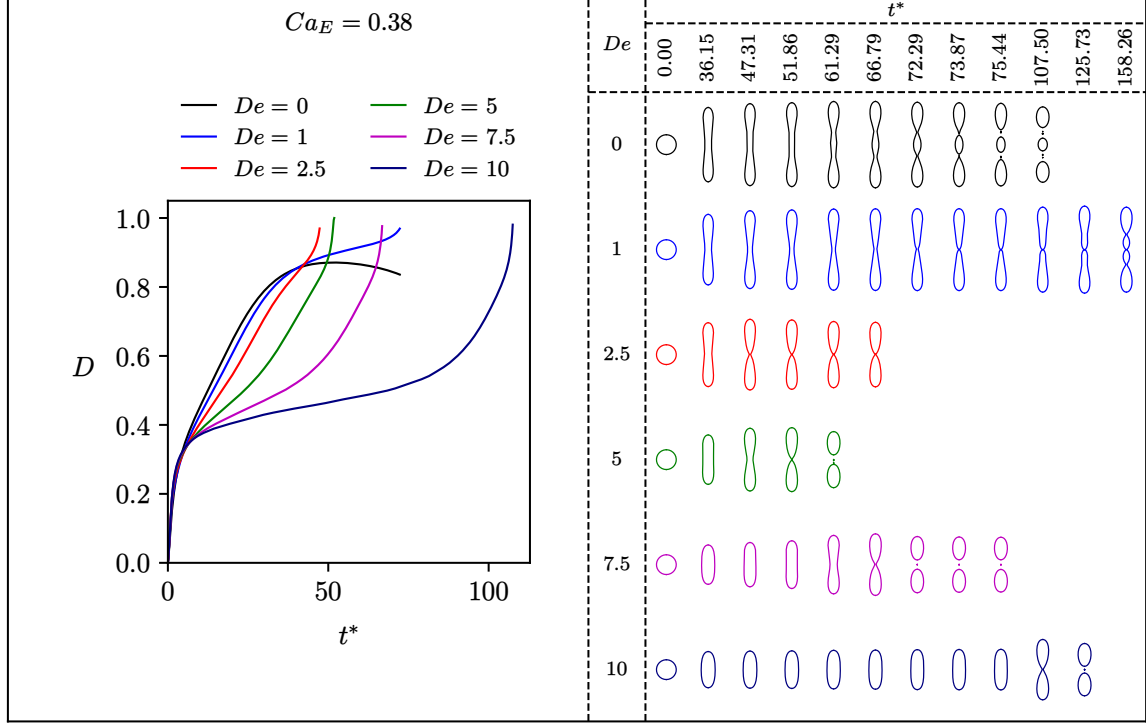


Figure 8: Evolution of drop interface with time for $\rho_r = 1$, $\mu_r = 1$, $Re = 1$, $\sigma_r = 10$, $\epsilon_r = 0.1$, $\beta_i = 1/9$, $\epsilon = 0.25$, $Ca_E = 0.38$. Deformation versus time is shown for each De till first pinch off.

temporal evolution of the drop interface, revealing more complex breakup patterns. At $Ca_E = 0.44$, the breakup behavior varies distinctly across different Deborah numbers (De). For $De = 0$, the drop elongates to form a three-lobed structure with a longer central lobe, which further breaks into three lobes, finally resulting in a central lobe with two-lobed structures at both ends. For $De = 1$, a three-lobed structure with a longer central lobe forms; the end lobes pinch off, and the central lobe subsequently breaks into three, leading to five attached lobes. At $De = 2.5$, the drop forms a four-lobed structure where the end lobes pinch off first, followed by the central two-lobed structure breaking into two attached two-lobed entities. When $De = 5$, the initial breakup is three-lobed and attached, where the end lobes then split further into two, resulting in five separated lobes. Finally, for $De = 7.5$ and 10 , an initial two-lobed breakup occurs; these lobes remain attached, with each subsequently breaking into two, yielding a total of four lobes (attached at $De = 7.5$ but separated at $De = 10$).

Similar to the previous case, a sharp increase in deformation precedes the initial breakup for $De = 7.5$ and $De = 10$, because of two lobed initial breakup. Overall, the initial number of breakup lobes decreases with increasing De (two for $De = 7.5, 10$ and three for $De \leq 5$). For initial three-lobed breakups, the central lobe length decreases with increasing De . This results in a three-lobed breakup of the central lobe at lower De (0,1), a two-lobed breakup at slightly higher $De = 2.5$, and breakup of the end lobes at $De = 5$ (where the central lobe is smaller than the end lobes). Interestingly, for the initial two-lobed breakups ($De = 7.5, 10$), the drop breaks up

number of lobes.

4.1.2. The drop behavior for $(\sigma_r, \epsilon_r) = (10, 1.37)$

Figure 10 illustrates the temporal evolution of a viscoelastic drop interface for $(\sigma_r, \epsilon_r) = (10, 1.37)$ across various electric capillary numbers (Ca_E) and Deborah numbers (De). Distinct color codes indicate different behaviors within the figure. A blue interface signifies a stable spheroidal equilibrium shape. For cases where the drop achieves stable multi-lobed configurations, the interface is shown in green at two intermediate time instances and at its final steady-state. When the drop undergoes breakup, the interface is depicted in red at two intermediate time instances and at the terminal simulation time. It is particularly interesting to note the cases shown in magenta: here, the drop initially deforms into a two-lobed shape and appears on the verge of breakup, but its neck recovers to form a three-lobed structure, which subsequently breaks into three daughter drops. Additionally, for the case highlighted in navy blue, the drop deforms into a two-lobed structure seemingly poised for pinch-off, yet it recovers to form a stable two-lobed configuration.

The stability of multi-lobed drop shapes is analyzed by examining streamlines and pressure contours, as illustrated in Figure 11. The streamlines and pressure contours are presented for a constant capillary number ($Ca_E = 0.4$) across three distinct Deborah numbers (De). For $De = 0$ and $De = 1$, which correspond to stable three-lobed and two-lobed drop configurations, respectively, the streamlines are observed to be tangential to the drop interface. The flow thus indicates a lack of interface motion, which is characteristic of a stable drop shape. Concurrently, organized internal flow patterns are observed, six recirculating eddies are present for $De = 0$, and four for $De = 1$. These coherent flow structures within the drop counteract the destabilizing capillary forces and prevent drop breakup. In contrast, at $De = 5$, the drop undergoes breakup. The streamlines and pressure field, for the time instance before the breakup, reveal a significant deviation from the stable state. In this unstable regime, the streamlines are no longer tangential to the interface, signifying interfacial motion. A high-magnitude outward velocity in the neck region of the deforming drop leads to the drop breakup.

Figure 12(a) presents the relationship between drop deformation and the electric capillary number for $(\sigma_r, \epsilon_r) = (10, 1.37)$ across various Deborah numbers. We observe two distinct behaviors based on the Deborah number range. For lower Deborah numbers ($De = 0, 1, 2.5$), the deformation curve exhibits two distinct branches. The lower branch corresponds to stable spheroidal deformation, up to a certain critical Ca_E . Beyond this critical value, the drop deforms into stable multi-lobed shapes, which are represented by the upper branch of the curve. In contrast, for higher Deborah numbers ($De = 5, 7.5, 10$), only a single branch of the deformation curve is observed. In these scenarios, the drop maintains a stable spheroidal shape up to a critical Ca_E , and upon exceeding this value, it undergoes breakup, thereby precluding the formation of stable multi-lobed shapes. Across all Deborah numbers, the lower branch of the deformation curve consistently exhibits a positive curvature. We also note that for a given Ca_E , the drop deformation is lower at higher Deborah numbers,

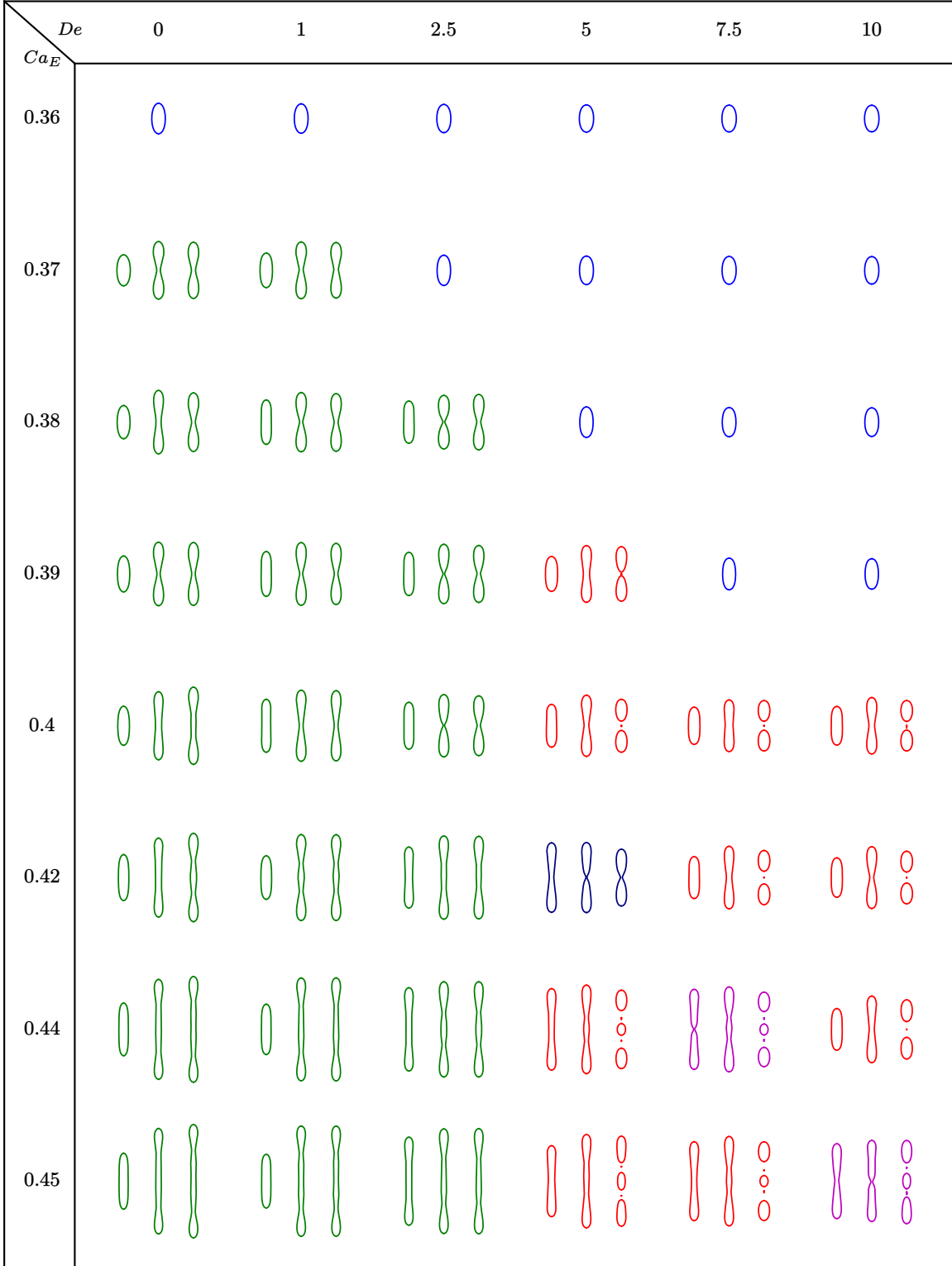


Figure 10: Behavior of drop interface in presence of electric field for various values of Ca_E and De for $(\sigma_r, \epsilon_r) = (10, 1.37)$, $\mu_r = 1$, $\rho_r = 1$, $Re = 1$, $\epsilon = 0.25$, $\beta_i = 1/9$

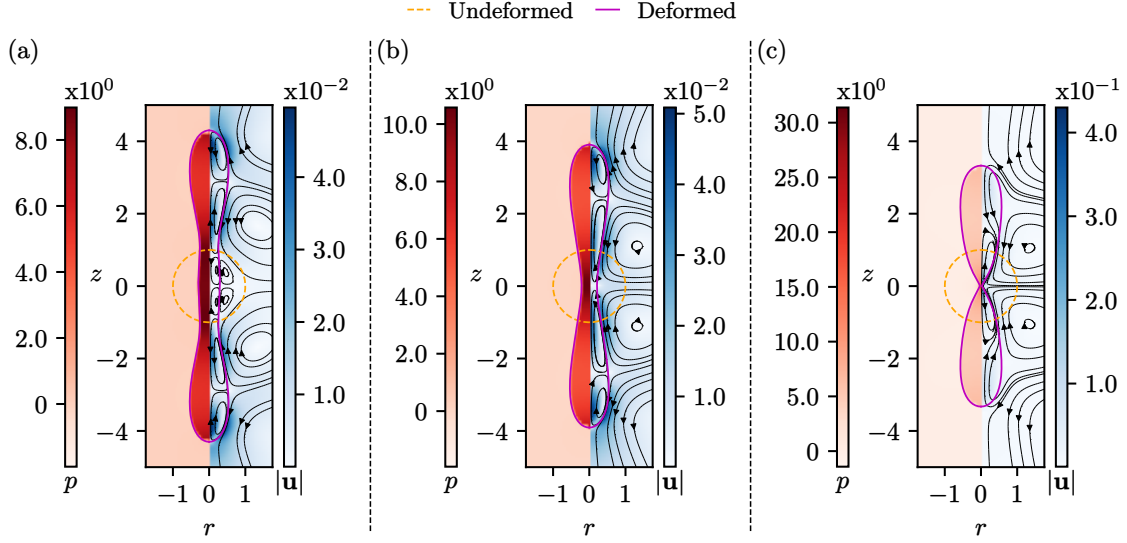


Figure 11: Streamlines and pressure contours for $Ca_E = 0.4$, $(\sigma_r, \epsilon_r) = (10, 1.37)$, $\mu_r = 1$, $\rho_r = 1$, $Re = 1$, $\epsilon = 0.25$, $\beta_i = 1/9$. (a) $De = 0$ (b) $De = 1$ (c) $De = 5$

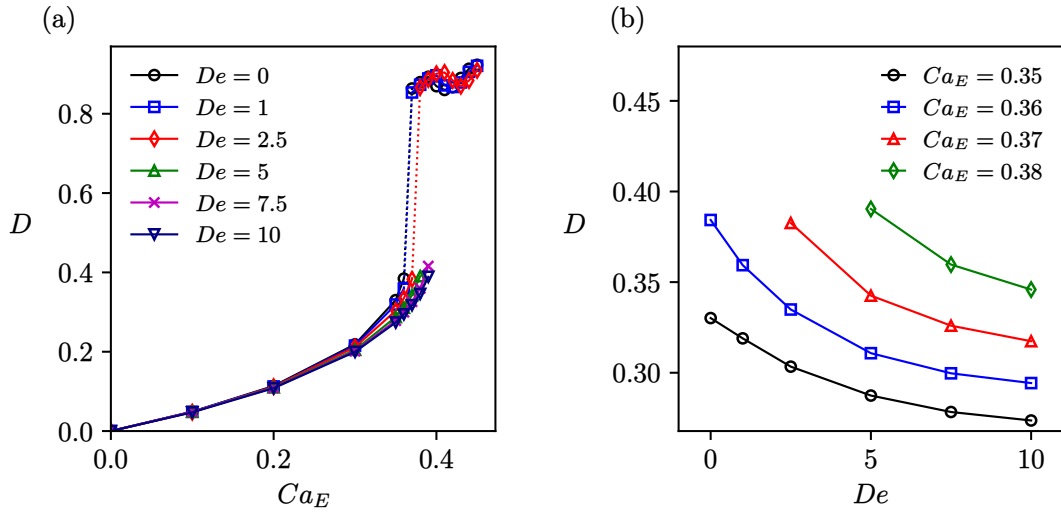


Figure 12: (a) Deformation versus Ca_E for various De , (b) Deformation versus De for various Ca_E , for $\rho_r = 1$, $\mu_r = 1$, $Re = 1$, $\sigma_r = 10$, $\epsilon_r = 1.37$, $\beta_i = 1/9$, $\epsilon = 0.25$. (from PR_A^+)

indicating a general decrease in drop deformation as De increases. This trend is further substantiated and clearly visible in Figure 12(b), which illustrates the direct dependence of deformation on the Deborah number. Moreover, Figure 12(b) also reveals that the drop deformation tends to saturate at higher values of the Deborah number.

Figure 13 presents the temporal evolution of the viscoelastic drop interface for multi-lobed breakup regimes ($De \geq 5$), as a function of the electric capillary number

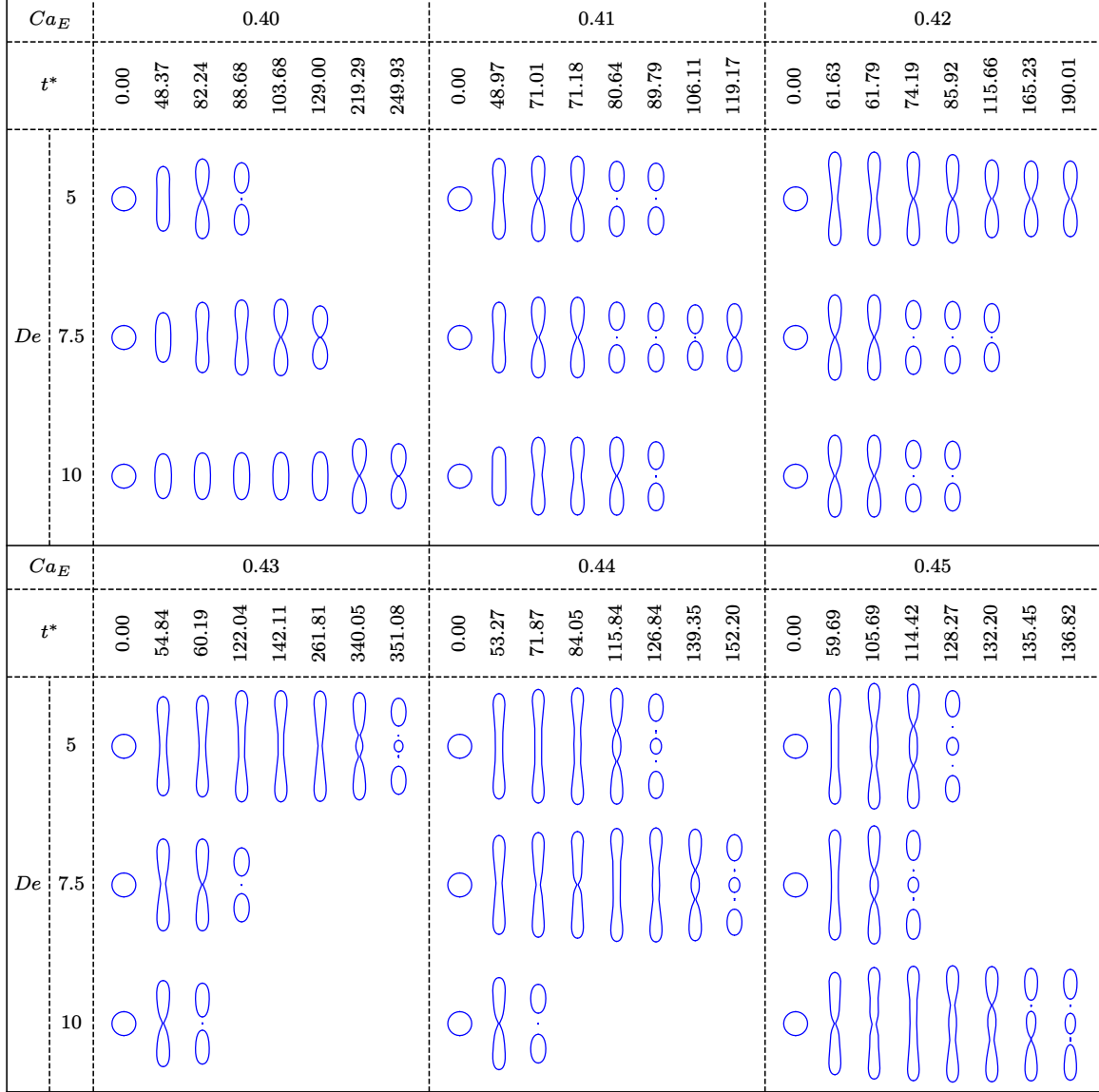


Figure 13: Temporal evolution of drop interface for $De = 5, 7.5, 10$ across the range of Ca_E for $\rho_r = 1$, $\mu_r = 1$, $Re = 1$, $\sigma_r = 10$, $\epsilon_r = 1.37$, $\beta_i = 1/9$, $\epsilon = 0.25$.

(Ca_E). At a lower Ca_E ($= 0.4$), the breakup time is observed to increase with De . However, at a slightly elevated $Ca_E = 0.41$, the overall breakup time decreases across all Deborah numbers examined. Specifically, $De = 5$ and $De = 7.5$ exhibit similar breakup times, while $De = 10$ shows a marginally longer breakup time compared to $De = 5$ and $De = 7.5$. Notably, at $Ca_E = 0.42$, for $De = 5$, the drop initially approaches a two-lobed breakup but then recovers to attain a stable two-lobed steady shape. For $Ca_E = 0.42$, drop exhibits two-lobed breakup for both $De = 7.5$ and 10 , with $De = 10$ showing a shorter breakup time than $De = 7.5$. In contrast, $De = 5$ undergoes a three-lobed breakup, which occurs at a longer breakup time. For $Ca_E = 0.44$, $De = 10$ still shows rapid two-lobed breakup, whereas $De = 7.5$ recovers

from a two lobed configuration on the verge of breakup, to undergo a three-lobed breakup with a longer breakup time than the three-lobed breakup of $De = 5$. At $Ca_E = 0.45$, the time taken for the three-lobed breakup decreases for both $De = 5$ and 7.5 , with a more pronounced reduction for $De = 7.5$, leading to a shorter breakup time compared to $De = 5$; and $De = 10$ transitions from a near two-lobed breakup to three-lobed shape and subsequently breaks into three daughter droplets. In summary, these observations reveal a nuanced influence of Deborah number on breakup time depending on the electric capillary number. Near the critical Ca_E for two-lobed breakup, higher De tends to delay breakup. However, as Ca_E increases beyond this critical value, the breakup time decreases more rapidly for higher values of De , suggesting an accelerating effect. A similar pattern is observed for three-lobed breakup: higher De delays breakup near the critical Ca_E for this mode, but accelerates it at higher Ca_E values.

4.2. The drop behavior for (σ_r, ϵ_r) from PR_B^+

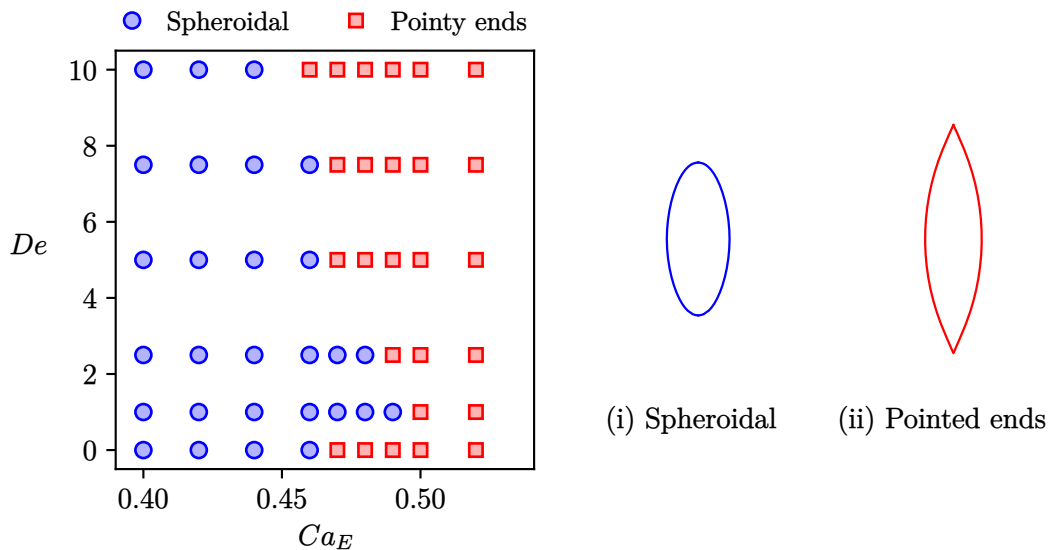


Figure 14: Phase plot on (Ca_E, De) plane representing the existence of spheroidal shapes and shapes with pointed ends

Similar to a Newtonian drop, a viscoelastic drop with (σ_r, ϵ_r) from the PR_B^+ region, when subjected to an electric field, deforms into a spheroidal shape up to a critical electric capillary number (Ca_E^{crit}). Beyond this threshold, the drop forms characteristic pointed-end shapes. Figure 14 illustrates this behavior as a phase diagram in the (Ca_E, De) plane. The diagram delineates regions of stable spheroidal shapes, marked by blue, from those forming pointed-end shapes (non-dimensional curvature of order 100), indicated by red markers. For Deborah numbers $De \geq 1$, the diagram distinctly shows that the maximum electric capillary number permitting a stable spheroidal shape decreases with increasing Deborah number.

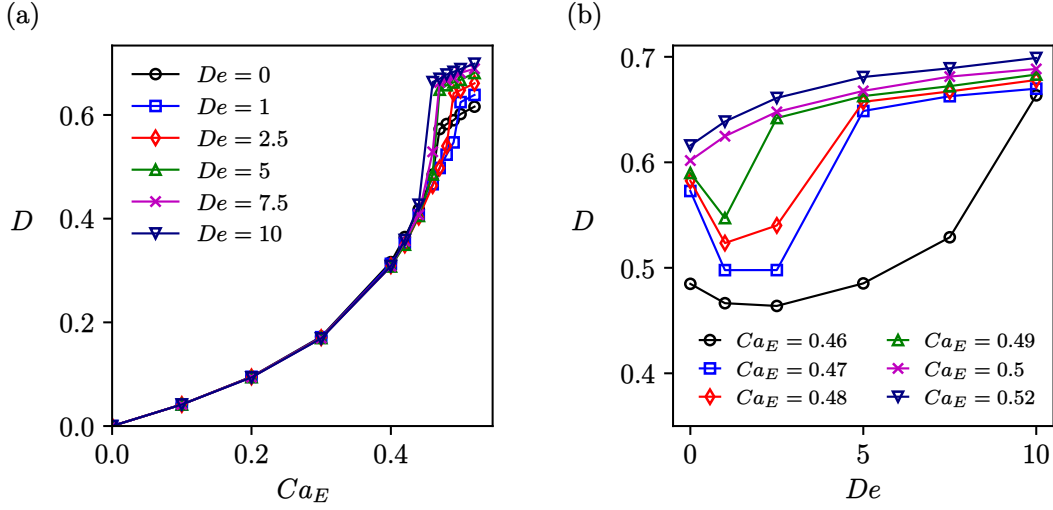


Figure 15: (a) Deformation versus Ca_E for various De , (b) Deformation versus De for various Ca_E , for $\rho_r = 1$, $\mu_r = 1$, $Re = 1$, $\sigma_r = 25$, $\epsilon_r = 50$, $\beta_i = 1/9$, $\epsilon = 0.25$. (from PR_B^+)

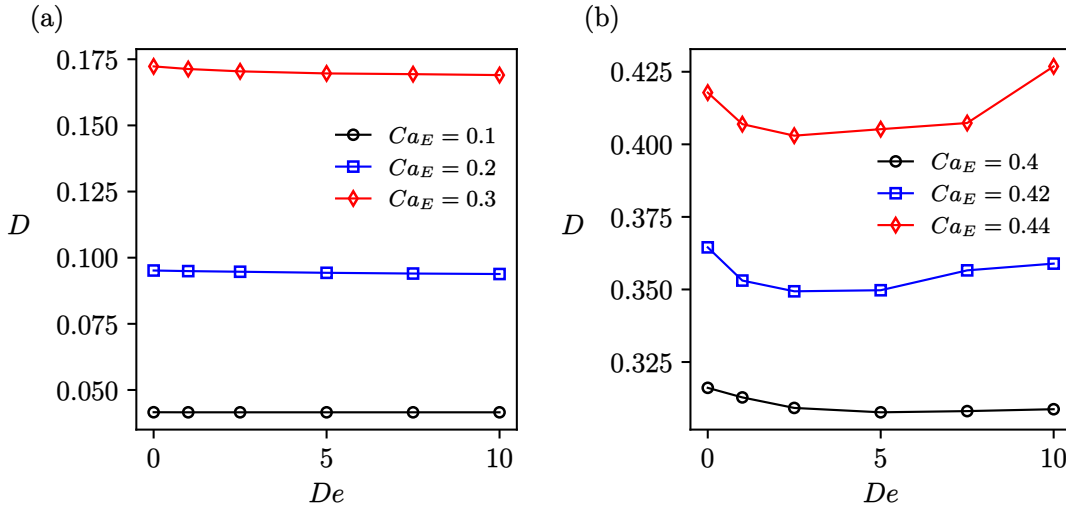


Figure 16: (a) Deformation versus De for various Ca_E for lower electric capillary numbers, (b) Deformation versus De for various Ca_E for intermediate electric capillary numbers, for $\rho_r = 1$, $\mu_r = 1$, $Re = 1$, $\sigma_r = 25$, $\epsilon_r = 50$, $\beta_i = 1/9$, $\epsilon = 0.25$. (from PR_B^+)

The influence of both the electric capillary number (Ca_E) and the Deborah number (De) on drop deformation is comprehensively illustrated in Figure 15 and 16. Figure 15(a) presents the variation of drop deformation with Ca_E across different De . For all Deborah numbers, deformation consistently increases with Ca_E . The concave upward nature of these deformation curves further indicates an accelerated increase in deformation at higher Ca_E . A notable feature observed for every De is a sudden jump in deformation at a certain critical Ca_E . This abrupt increase signi-

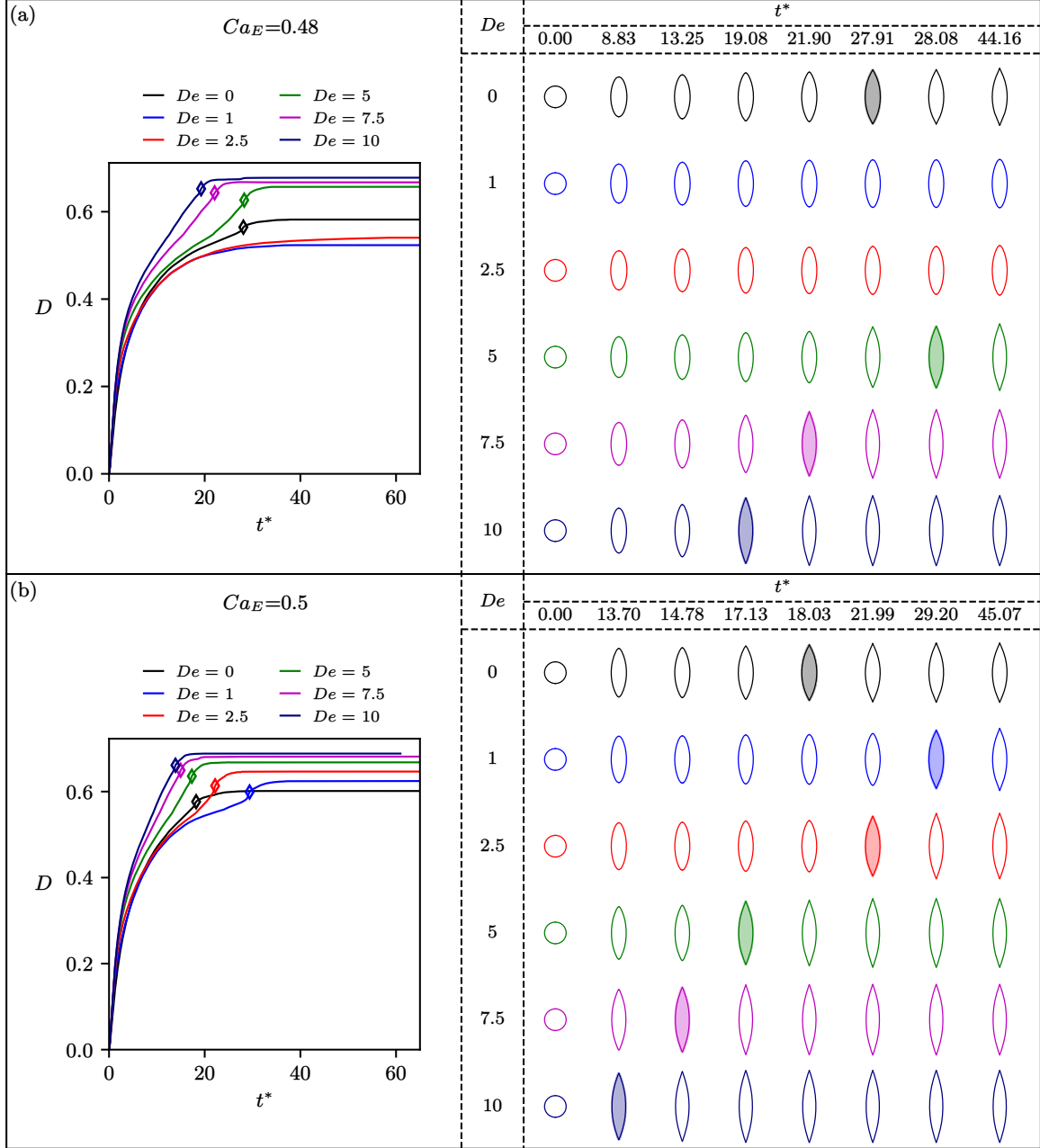


Figure 17: Variation of deformation parameter with time and temporal evolution of drop interface for various De for $\rho_r = 1$, $\mu_r = 1$, $Re = 1$, $\sigma_r = 25$, $\epsilon_r = 50$, $\beta_i = 1/9$, $\epsilon = 0.25$. (a) $Ca_E = 0.48$ (b) $Ca_E = 0.5$. Markers on each D versus t^* indicates the time at which drop transforms to the shape characterized by the pointy ends. Interface shape corresponding to the diamond marker is filled with the lighter shade of the corresponding color.

fies the transition from a stable spheroidal shape to a more elongated configuration with pointed ends, after which deformation continues to increase at a nearly constant rate with Ca_E . Figure 15(b) illustrates drop deformation variation with De for several higher Ca_E values, specifically those where the drop exhibits pointed ends for

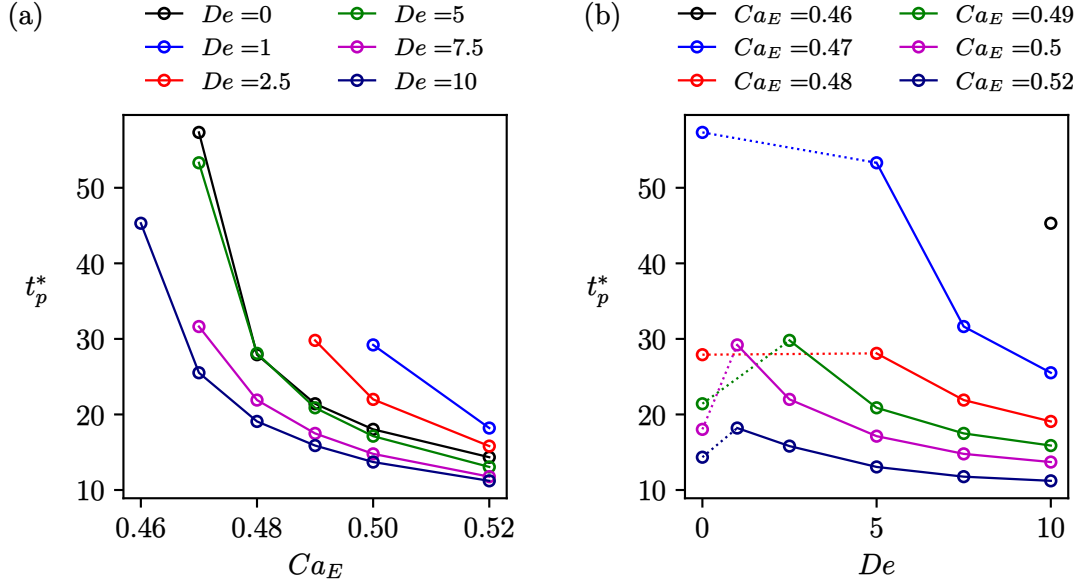


Figure 18: (a) The variation of time that is required for the formation of pointed ends with Ca_E . (b) Time of formation of pointed ends versus De for $\rho_r = 1$, $\mu_r = 1$, $Re = 1$, $\sigma_r = 25$, $\epsilon_r = 50$, $\beta_i = 1/9$, $\epsilon = 0.25$.

at least one De . For $Ca_E \geq 0.5$, where the drop consistently deforms into shapes with pointed ends across all De , deformation is observed to increase gradually with De . The behavior is non-monotonic at $Ca_E = 0.46$: deformation initially decreases, then increases with increasing De . It is crucial to note that at $Ca_E = 0.46$, the drop forms pointed ends exclusively at $De = 10$, resulting in the highest deformation for $De = 10$. For intermediate Ca_E values (0.47, 0.48, 0.49), pointed ends appear for $De = 0$ and also at higher De , while for some intermediate De values drop maintains stable spheroidal shape. Further insights into the dependence of drop deformation on De for low to moderate Ca_E are provided in Figure 16. Specifically, Figure 16(a) illustrates the deformation vs. De at very low Ca_E , revealing a minimal sensitivity of drop deformation to variations in De , characterized by a slight decrease in deformation with De . In contrast, Figure 16(b) depicts the drop deformation as a function of De for moderate Ca_E . This regime exhibits a non-monotonic relationship, where droplet deformation initially decreases with increasing De , followed by a subsequent increase.

Figure 17 presents the temporal evolution of droplet deformation and the corresponding interfacial dynamics for varying Deborah numbers at two distinct electric capillary numbers, $Ca_E = 0.48$ and 0.5. Diamond markers on the deformation versus time curves indicate the transition of drop shape from spheroidal to the shape with pointed ends. The shape of the interface corresponding to this time is filled by the lighter shade of the corresponding color. At $Ca_E = 0.48$, shapes with pointed ends are observed for $De = 0, 5, 7.5, 10$, with $De = 1$ and 2.5 resulting in stable spheroidal configurations. For $De \geq 5$ at this Ca_E , the transition to a pointed end shape occurs

earlier with increasing De , while the transition time for $De = 0$ is intermediate between $De = 5$ and 7.5 . At a higher $Ca_E = 0.5$, all investigated De values exhibit a transition to the shapes with pointed ends. For $De \geq 1$ at $Ca_E = 0.5$, the transition time decreases with increasing De , and the transition time for $De = 0$ is intermediate between $De = 2.5$ and $De = 5$.

Figure 18(a) and (b) illustrate the dependence of the dimensionless transition time to a shape with pointed ends, denoted as t_p^* , on the electric Capillary number (Ca_E) and the Deborah number (De), respectively. From Figure 18(a), a monotonic decrease in t_p^* with increasing Ca_E is evident across all De , signifying an accelerated transition to the shapes with pointed ends at higher electric field strengths. Figure 18(b) reveals that for $De \geq 1$, t_p^* decreases with increasing De , indicating a faster onset of drop shapes with pointed ends at higher Deborah numbers. However, the transition time for $De = 0$ is comparable to that observed for $De = 5$. This proximity is further corroborated by the near overlap of the t_p^* versus Ca_E curves for $De = 0$ and $De = 5$ in Figure 18(a).

4.3. The drop behavior (σ_r, ϵ_r) from OB^-

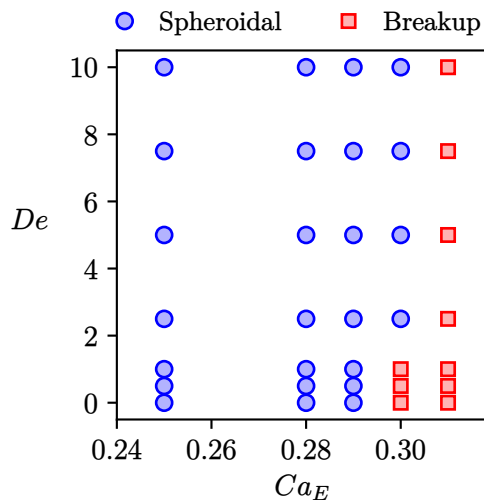


Figure 19: Phase plot on (Ca_E, De) plane representing the existence of stable deformed shapes and drop breakup

Similar to its Newtonian counterpart, a viscoelastic drop subjected to an external electric field, for $(\sigma_r, \epsilon_r) = (0.1, 2)$ corresponding to the OB^- region, undergoes oblate deformation up to a critical electric capillary number, and beyond this critical Ca_E , the drop loses its stability and experiences electrohydrodynamic breakup. Figure 19 presents a phase diagram in the (Ca_E, De) plane, delineating the steady-state drop shape and drop breakup regimes. The blue markers denote the existence of stable, steady-state oblate drop shapes, while the red markers denote the occurrence of drop breakup. For lower Deborah numbers ($De = 0, 0.5$, and 1), drop breakup is observed

at an electric capillary number of $Ca_E = 0.3$. In contrast, for higher Deborah numbers ($De = 2.5, 5, 7.5$, and 10), the drop attains a stable oblate shape at $Ca_E = 0.3$, with breakup occurring at a slightly elevated electric capillary number of $Ca_E = 0.31$.

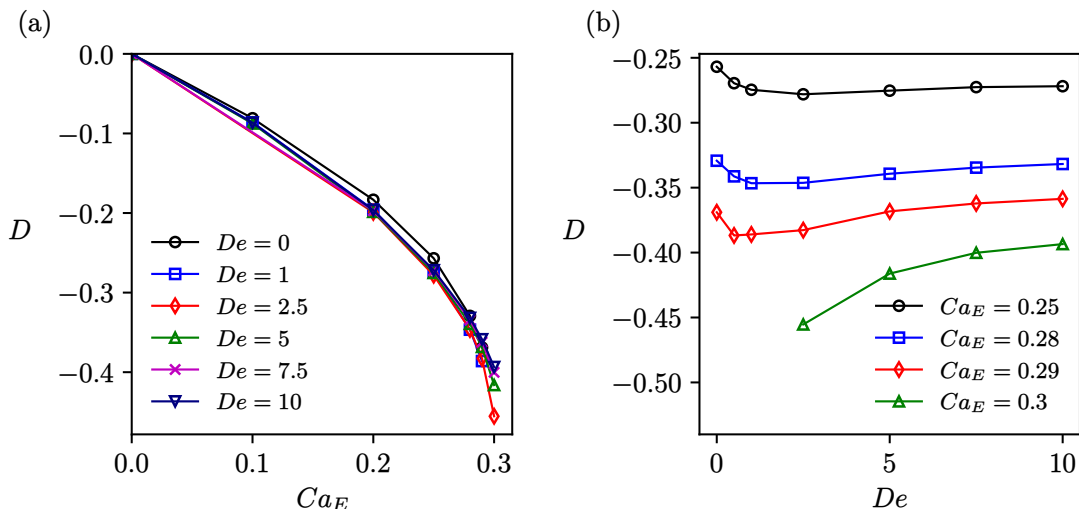


Figure 20: (a) Deformation versus Ca_E for various De , (b) Deformation versus De for various Ca_E , for $\rho_r = 1$, $\mu_r = 1$, $Re = 1$, $\sigma_r = 0.1$, $\epsilon_r = 2$, $\beta_i = 1/9$, $\epsilon = 0.25$. (from OB^-)

Figure 20 illustrates the dependence of the drop deformation parameter on the electric capillary number (Ca_E) and the Deborah number (De). Specifically, Figure 20(a) depicts the evolution of the drop deformation parameter as a function of the electric capillary number for several Deborah numbers. The results indicate that the magnitude of the drop deformation increases with increasing electric capillary number. Consistent with the Newtonian case, the rate of increase in the magnitude of deformation with respect to Ca_E remains positive across the investigated range of Deborah numbers. Figure 20(b) presents the variation of the drop deformation parameter with the Deborah number for various electric capillary numbers. An interesting non-monotonic behavior of the deformation parameter with the Deborah number is observed. An initial increase in the magnitude of drop deformation is observed with an increase in the Deborah number, for a fixed electric capillary number, up to a certain De threshold, beyond which the magnitude of deformation begins to decrease. For example, at $Ca_E = 0.25$, the magnitude of the deformation increases with De until $De = 2.5$, followed by a subsequent decrease. Similarly, at $Ca_E = 0.28$, the magnitude of the deformation increases until $De = 1$ and then decreases. For $Ca_E = 0.29$, the magnitude of the deformation increases with De up to $De = 0.5$ and decreases thereafter. In particular, at $Ca_E = 0.3$, stable droplet shapes are not attainable at lower Deborah numbers ($De = 0, 0.5$ and 1), and for higher Deborah numbers where steady states are observed, the magnitude of deformation decreases with increasing De . A similar non-monotonic behavior has been observed by Aggarwal and Sarkar (2008) for the shear-induced deformation of a drop in viscoelastic

matrix.

For lower Ca_E , increase in magnitude of deformation is observed upto higher values of De , before it starts to decrease. For example, for $Ca_E = 0.25$, magnitude of deformation increases with De till $De = 2.5$ before it starts to decrease. whereas, for $Ca_E = 0.29$, magnitude of deformation increases with De till $De = 0.5$ and then it shows increase with De . Similarly, for $Ca_E = 0.28$, magnitude of deformation increases with De till $De = 1$ and then it starts to decrease. At $Ca_E = 0.3$, drop cannot achieve stable shapes for lower De ($De = 0, 0.5$ and 1), and magnitude of deformation decreases with De for higher De , where steady shapes are observed.

Figure 21 illustrates the temporal evolution of droplet deformation and interfacial morphology for varying Deborah numbers (De) at four distinct electric capillary numbers, $Ca_E = 0.3, 0.31, 0.32, 0.35$ for the pair of $(\sigma_r, \epsilon_r) = (0.1, 2)$ from OB^- region. At $Ca_E = 0.3$, stable oblate droplet configurations are observed for $De \geq 2.5$, while instability and breakup occur for lower Deborah numbers ($De = 0, 0.5, 1$). The characteristic breakup time increases with De in the unstable regime, indicating viscoelastic retardation of the breakup. The deformation versus dimensionless time curves, truncated at the point of breakup, exhibit a sharp decrease in deformation immediately preceding the breakup, thus defining the breakup time. For $Ca_E = 0.31$, drop breakup is observed across the investigated De range. For $De \geq 0.5$, the breakup time increases with De , while the breakup time for $De = 0$ is marginally greater than that for $De = 0.5$. A similar trend is evident at $Ca_E = 0.32$, with increasing breakup times with De for $De \geq 0.5$ and an increase in breakup time as De decreases from 0.5 to 0 . Notably, the breakup times for $De = 0$ and $De = 1$ are comparable. At the highest investigated electric Capillary number, $Ca_E = 0.35$, a similar dependence of breakup time on De is observed, with the breakup time generally increasing with De for $De \geq 0.5$. Furthermore, the breakup time for $De = 0$ is greater than that for $De = 1$. We also note that the decrease in breakup time for a fixed De with increasing Ca_E .

To elucidate the dependence of the dimensionless droplet breakup time on the electric Capillary number (Ca_E) and the Deborah number (De), Figure 22(a) and (b) illustrate the respective variations. Figure 22(a) reveals a monotonic inverse relationship between the breakup time and Ca_E across all examined De . Conversely, Figure 22(b) demonstrates a monotonic increase in breakup time with De at $Ca_E = 0.3$. However, for $Ca_E \geq 0.31$, a slight decrease is observed in the breakup time as De increases from 0 to 0.5 , followed by a monotonic increase in breakup time with further increments in De . Notably, the maximum investigated Deborah number ($De = 10$) exhibits a significantly higher rate of decrease in breakup time with increasing electric capillary number (Ca_E) compared to lower De values. Consequently, at the maximum investigated $Ca_E = 0.35$, the breakup times across the different Deborah numbers converge to comparable values, indicating a diminishing influence of viscoelasticity on the breakup dynamics at higher electric field strengths.

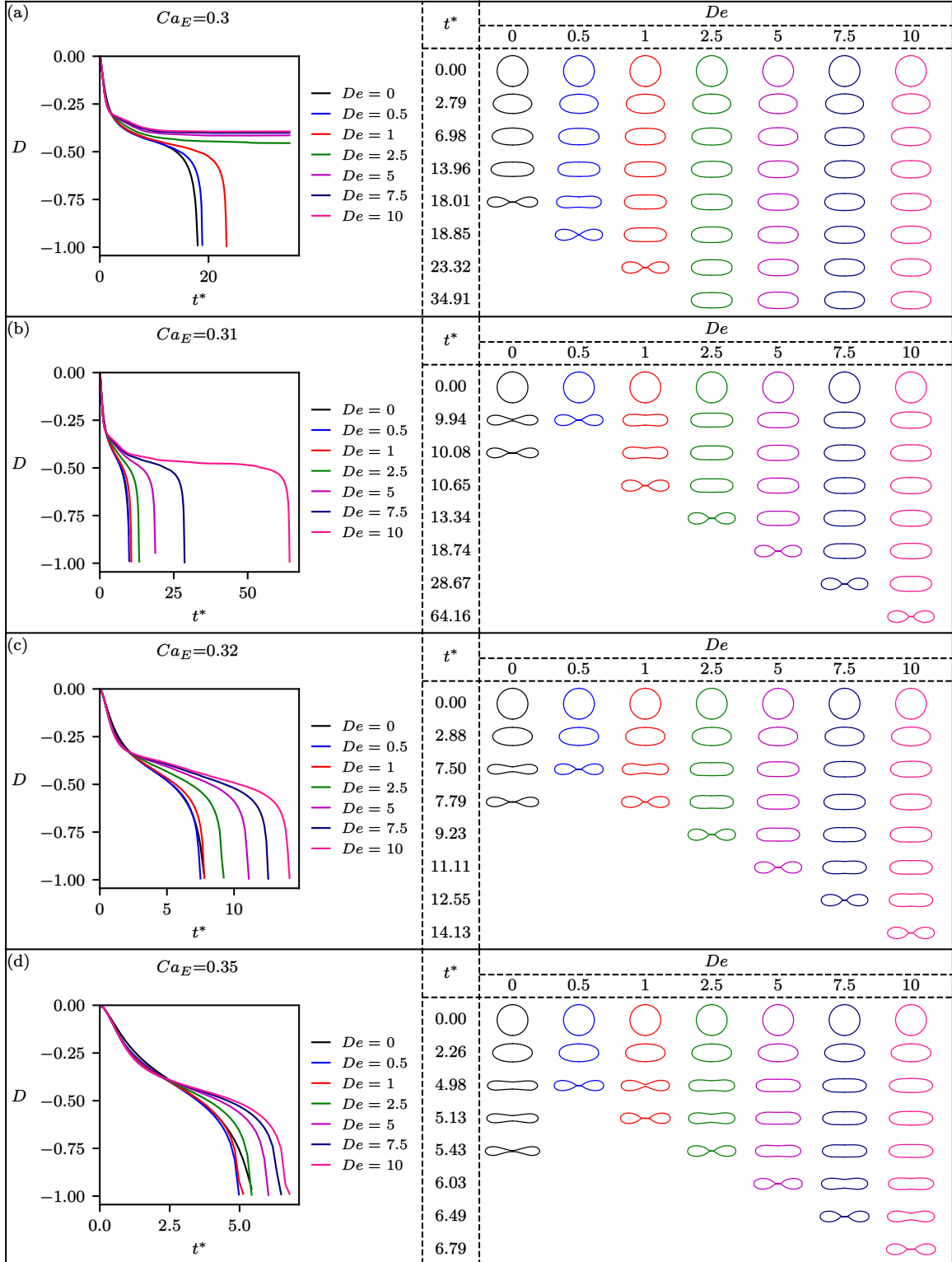


Figure 21: The variation of drop deformation with time and the evolution of the drop interface for various Deborah numbers for $\rho_r = 1$, $\mu_r = 1$, $Re = 1$, $\sigma_r = 0.1$, $\epsilon_r = 2$, $\beta_i = 1/9$, $\epsilon = 0.25$. (a) $Ca_E = 0.3$ (b) $Ca_E = 0.31$ (c) $Ca_E = 0.32$ (d) $Ca_E = 0.35$

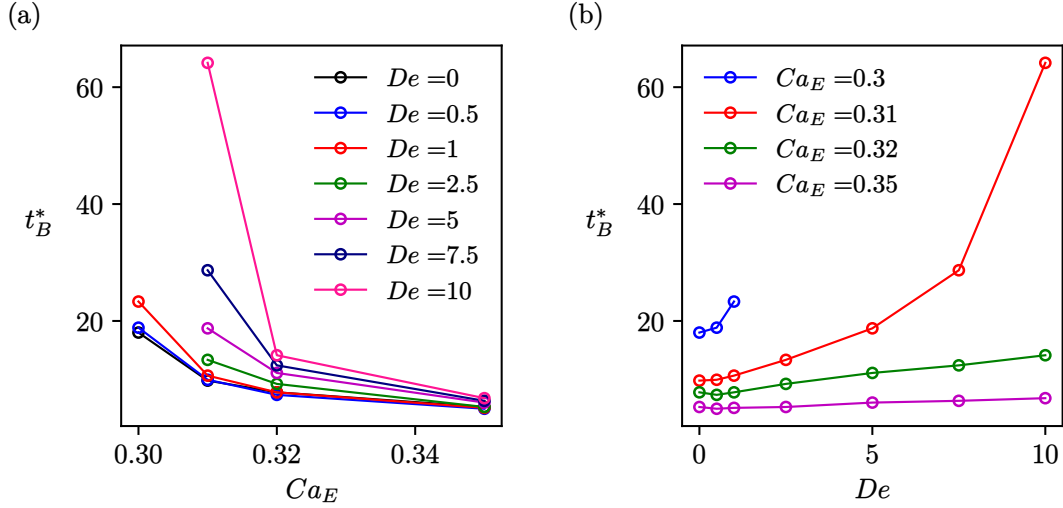


Figure 22: The variation of breakup time with (a) Ca_E and (b) De for $\rho_r = 1$, $\mu_r = 1$, $Re = 1$, $\sigma_r = 0.1$, $\epsilon_r = 2$, $\beta_i = 1/9$, $\epsilon = 0.25$.

4.4. Comparison with Oldroyd-B drops

The Oldroyd-B and Linear Phan-Thien-Tanner (LPTT) models differ fundamentally in how they predict stress growth under extension. In the Oldroyd-B model, the polymer stress evolves linearly with the deformation rate, which causes the extensional viscosity to diverge at a finite rate of extension, reflecting the unbounded stress growth associated with the assumption of infinitely extensible Hookean springs. In contrast, the LPTT model modifies the constitutive equation by introducing a non-linear damping function,

$$f(\text{tr } \tau_p) = 1 + \epsilon \frac{\lambda}{\eta_p} \text{tr } \tau_p, \quad (18)$$

which effectively limits the increase of stress at large deformation rates. Consequently, while Oldroyd-B predicts unphysical divergence in stress and extensional viscosity, the LPTT model exhibits strain-hardening at moderate De and self-limiting stress at high De , representing the finite extensibility of polymer chains and offering a more realistic description of viscoelastic fluid behavior under strong extensional or electric stresses.

In the PR_A^+ region, for $(\sigma_r, \epsilon_r) = (10, 1.37)$, both Oldroyd-B (refer to [Bangar and Tomar \(2026\)](#)) and LPTT drops deform into prolate shapes, with internal flow directed from the equator to the poles. The overall electrohydrodynamic behavior of Oldroyd-B and LPTT drops exhibits notable similarities with a few key differences when $(\sigma_r, \epsilon_r) = (10, 1.37)$. Both fluid types demonstrate a critical electric capillary number (Ca_E), below which the drop deforms to a stable spheroidal shape. A crucial distinction arises beyond this critical Ca_E : Oldroyd-B drops consistently deform into stable multi-lobed shapes across all Deborah numbers (De) investigated, as discussed in [Bangar and Tomar \(2026\)](#). Conversely, LPTT drops form stable multi-lobed shapes only at low De values ($De = 0, 1, 2.5$), while they tend to break up at higher De ($De =$

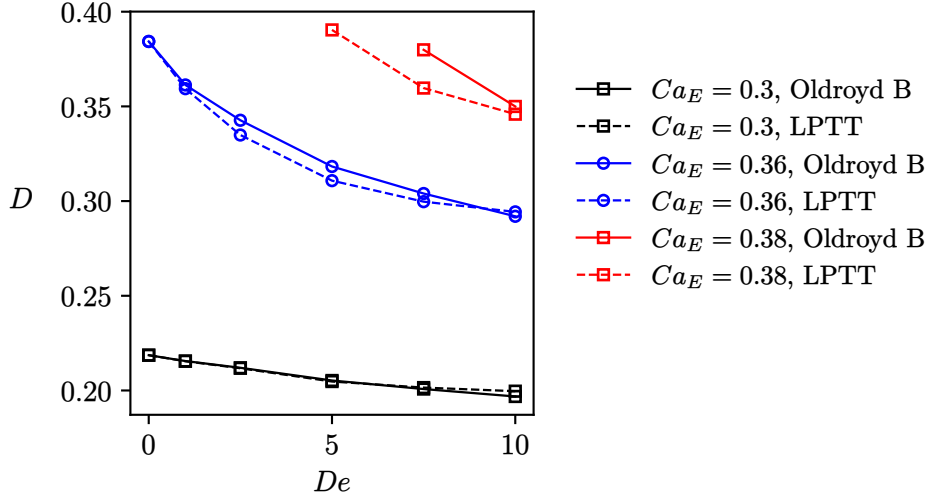


Figure 23: Deformation versus De for various Ca_E , for $\rho_r = 1$, $\mu_r = 1$, $Re = 1$, $\sigma_r = 10$, $\epsilon_r = 1.37$, $\beta_i = 1/9$, $\epsilon = 0.25$ for LPTT model

5, 7.5, 10). An exception to this LPTT breakup at high De is observed at $Ca_E = 0.42$ and $De = 5$, where the drop recovers from necking to form a stable two-lobed shape. For the both Oldroyd-B and LPTT models, drop deformation decreases monotonically with increasing De . Figure 23 provides a detailed comparison of deformation versus De for Oldroyd-B and LPTT drops at three distinct Ca_E values: 0.3, 0.36, and 0.38. This analysis specifically focuses on conditions where both fluid types form stable spheroidal shapes. At $Ca_E = 0.3$, the deformation vs. De curves for both Oldroyd-B and LPTT drops show nearly overlapping behavior for $De \leq 7.5$. However, at $De = 10$, the LPTT drop exhibits a very slightly higher deformation compared to the Oldroyd-B drop. Moving to $Ca_E = 0.36$, the deformations are almost identical for both fluids at both low and high De values. For intermediate De values ($De = 2.5, 5, 7.5$), the deformation of LPTT drop is marginally lower. Here, both electric and hydrodynamic stresses elongate the drop, while elastic stresses resist stretching, leading to decreasing deformation with increasing De . Because electric stresses are relatively weak and uniform for this set of conductivity and permittivity ratios, non-linear damping in the LPTT model is minor, resulting in similar deformation trends for both models.

In the PR_B^+ region, for $(\sigma_r, \epsilon_r) = (25, 50)$, the drop assumes a prolate shape, but the internal flow reverses direction and it is from the poles toward the equator. Here, the hydrodynamic stress opposes the electric stress, yet the latter dominates, driving prolate deformation. When comparing the behavior of Oldroyd-B and LPTT drops under a steady electric field, distinct differences in their time evolution are evident. the deformation of an LPTT drop monotonically increases with time until it reaches a steady-state value. In contrast, for higher Deborah numbers (De), the deformation of an Oldroyd-B drop (see: [Bangar and Tomar \(2026\)](#)) typically exhibits a more complex

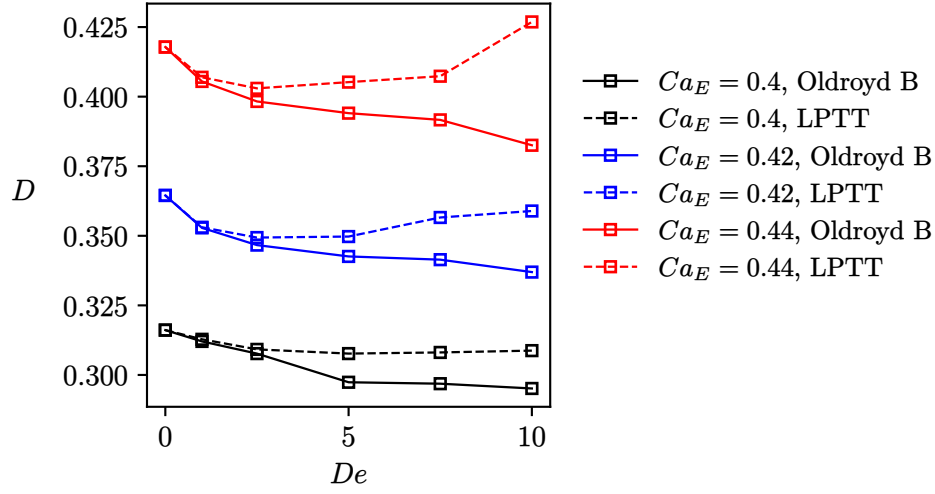


Figure 24: Variation of deformation parameter with De for various Ca_E for $\rho_r = 1$, $\mu_r = 1$, $Re = 1$, $\sigma_r = 25$, $\epsilon_r = 50$, $\beta_i = 1/9$

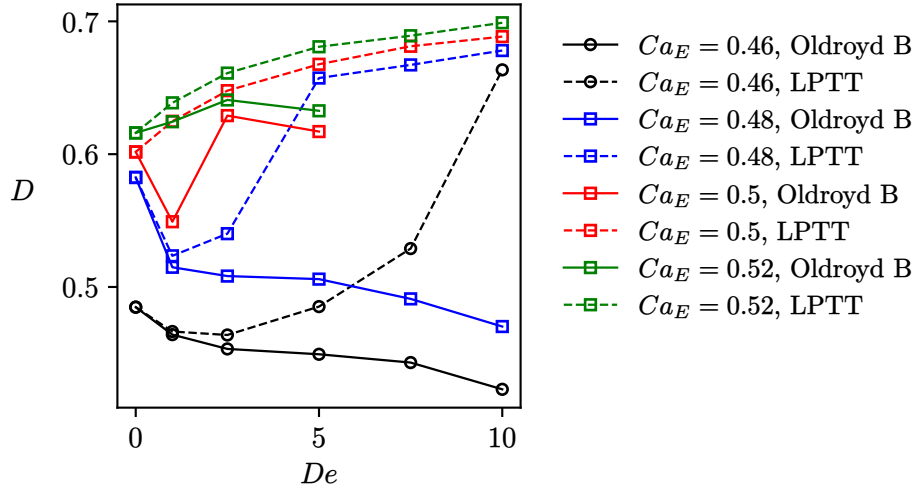


Figure 25: Variation of deformation parameter with De for various Ca_E for $\rho_r = 1$, $\mu_r = 1$, $Re = 1$, $\sigma_r = 25$, $\epsilon_r = 50$, $\beta_i = 1/9$

transient behavior. It often passes through a maximum deformation before settling into a steady state, sometimes even undergoing a subsequent minimum. For example, at $Ca_E = 0.48$, the drop deformation shows both a maximum and a minimum before reaching its steady-state value, even though the drop shape consistently remains spheroidal. Furthermore, in certain scenarios, the Oldroyd-B drop can transiently deform into a pointed shape during its maximum deformation phase, subsequently

returning to a spheroidal steady state after passing through a minimum. This is observed for $De = 10$ at $Ca_E = 0.5$ and $Ca_E = 0.52$. In some cases, such as for $De = 7.5$ at $Ca_E = 0.5$ and 0.52 , the drop may even oscillate between pointed and spheroidal shapes without achieving a stable steady state. To compare the influence of the Deborah number (De) on the electrohydrodynamic deformation of Oldroyd-B and LPTT drops, [Figure 24](#) and [Figure 25](#) illustrate the variation of steady-state deformation with De for both fluid types across various electric capillary numbers (Ca_E). [Figure 24](#) reveals that for moderate Ca_E values (0.4, 0.42, 0.44), the steady-state deformation of an Oldroyd-B drop is consistently lower than that of an LPTT drop across all non-zero De values examined. A key distinction in their deformation behavior is observed: the LPTT drop exhibits non-monotonic deformation with respect to De , whereas the Oldroyd-B drop's deformation monotonically decreases with increasing De . Furthermore, as Ca_E increases, the difference in steady-state deformation between the two fluid models widens. These differences arise from the stronger and more localized electric stresses near the poles in this high-conductivity, high-permittivity region PR_B^+ . The intense extension activates nonlinear stress responses in the LPTT model, initial strain hardening at moderate De , followed by stress saturation at large De . Consequently, LPTT drops exhibit a non-monotonic dependence of deformation on De , while Oldroyd-B drops display a steady decline in deformation with increasing elasticity. [Figure 25](#) extends this comparison to higher Ca_E values (0.46, 0.48, 0.5, 0.52). At $Ca_E = 0.46$, the gap in deformation between the two models further increases, with the LPTT drop deforming to a pointed shape at $De = 10$, while the Oldroyd-B drop maintains a spheroidal steady shape. As Ca_E increases to 0.48, the LPTT drop forms pointed shapes for $De \geq 5$ and also for $De = 0$ (corresponding to Newtonian behavior), while the Oldroyd-B drop continues to deform into stable, spheroidal steady shapes for all non-zero De . For $Ca_E \geq 0.5$, the LPTT drop consistently deforms into a pointed shape across all De . Conversely, the Oldroyd-B drop achieves pointed steady shapes for all $De \leq 5$ (with an exception at $De = 1$ for $Ca_E = 0.5$), and for all $De \leq 5$ at $Ca_E = 0.52$. Examining the conditions (Ca_E and De) under which drops deform into pointed steady shapes, we observe that for LPTT drops, deformation consistently increases with De . However, for Oldroyd-B drops, the deformation in pointed shapes exhibits non-monotonic dependence on De : it increases as De rises from 0 to 2.5, then decreases as De further increases to 5. Interestingly, for Oldroyd-B fluids at $De \geq 7.5$, steady pointed shapes are not achieved. Instead, the drop either oscillates between pointed and spheroidal shapes or transiently forms a pointed shape before settling into a spheroidal steady state as observed by [Bangar and Tomar \(2026\)](#).

In the OB^- region, the drop attains an oblate shape due to the electric field (for the selected conductivity ratio and permittivity ratio electric field tends to deform drop to oblate shape as described by [Esmaeeli and Behjatian \(2020\)](#)), with the flow directed from the poles toward the equator. Comparing the behavior of Oldroyd-B drops (discussed in [Bangar and Tomar \(2026\)](#)) with LPTT drops in a steady electric field reveals significant differences, even with some shared characteristics. Consistent with Newtonian fluid behavior, both Oldroyd-B and LPTT drops exhibit a critical

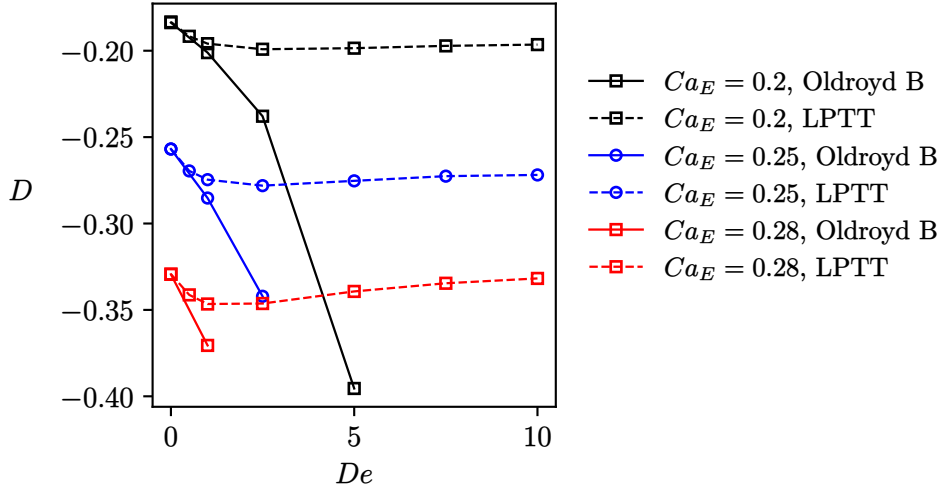


Figure 26: (a) Deformation versus Ca_E for various De , (b) Deformation versus De for various Ca_E , for $\rho_r = 1$, $\mu_r = 1$, $Re = 1$, $\sigma_r = 0.1$, $\epsilon_r = 2$, $\beta_i = 1/9$, $\epsilon = 0.25$ for LPTT model. (from OB^-)

electric capillary number (Ca_E). Below this value, the drop can deform into a stable shape; exceeding it leads to breakup. However, their stable deformation modes differ. LPTT drops deform to a stable spheroidal shape when Ca_E is below its critical value. In contrast, Oldroyd-B drops, while mainly forming stable spheroidal shapes below critical Ca_E , can also form stable shapes with dimples ($Ca_E = 0.2$, $De = 5$). In some instances (specifically at low Ca_E and high De , for example, $De \geq 7.5$ for $Ca_E = 0.1$ and 0.2), Oldroyd-B drops can even form dimples and attempt to break up, only to recover into a spheroidal shape and undergo positional oscillations. Furthermore, LPTT drops generally demonstrate greater stability, showing a higher critical Ca_E at elevated De values. Oldroyd-B drops, on the contrary, show a lower critical Ca_E for higher De . It is important to note that the LPTT drops do not breakup for any De up to $Ca_E = 0.28$. However, Oldroyd-B drops experience breakup for $De \geq 2.5$ at $Ca_E = 0.28$, and for $Ca_E = 0.25$, breakup occurs at $De \geq 5$. Although Oldroyd-B drops do not breakup at $Ca_E = 0.2$ for any De , for $De \geq 7.5$, they attempt to break and then recover, leading to positional oscillations. Regarding breakup kinetics, LPTT drops generally take longer to break up at higher De , whereas Oldroyd-B drops break up more quickly under similar conditions. Figure 26 illustrates the variation of the deformation parameter with De for Oldroyd-B and LPTT drops at three values of Ca_E : 0.2, 0.25, and 0.28. The deformation parameter (magnitude of deformation) for LPTT drops exhibits non-monotonic behavior, initially decreasing (increasing) and then increasing (decreasing) with De . Conversely, for Oldroyd-B drops, it monotonically decreases (increases) with De . The magnitude of deformation is significantly higher for Oldroyd-B drops compared to LPTT drops. Thus, for Oldroyd-B drops, increasing De generally enhances drop deformation and leads to earlier breakup. In contrast, LPTT drops display a non-monotonic response where

the magnitude of deformation initially increases due to strain hardening and then decreases at larger De owing to stress saturation, indicating greater resistance to deformation and breakup at high De values.

5. Conclusion

The deformation and breakup dynamics of a linear PTT drop under an electric field are numerically investigated and compared with those of Oldroyd-B drops. Representative pairs of conductivity (σ_r) and permittivity (ϵ_r) ratios are selected from six regions of the (σ_r, ϵ_r) phase plot, PR_A^+ , PR_B^+ , PR_A^- , PR_B^- , OB^- , and OB^+ . For (σ_r, ϵ_r) pairs within PR_A^- , PR_B^- , and OB^+ regions, drop deformation increases gradually with the electric capillary number (Ca_E), leading to smooth shape evolution and stable steady states even at high Ca_E . In these regions, viscoelastic effects are minimal.

For (σ_r, ϵ_r) pair within the PR_A^+ region, an LPTT drop deforms into a stable spheroidal shape when the electric capillary number (Ca_E) is below a critical value. Beyond this critical Ca_E , the drop forms stable multi-lobed shapes or breaks up. Drop deformation decreases with increasing Deborah number (De), indicating an enhanced resistance to deformation with increasing viscoelasticity. The overall behavior closely resembles that of an Oldroyd-B drop, with some notable distinctions. At both low and high De , the deformation of Oldroyd-B and LPTT drops is nearly identical. However, for intermediate De values, Oldroyd-B drops exhibit slightly higher deformation than LPTT drops. Furthermore, the critical Ca_E for Oldroyd-B drops is observed to be slightly lower than or similar to that of LPTT drops, depending on De .

In the PR_B^+ region, LPTT drops deform into a steady spheroidal shape up to a critical Ca_E and forms shapes with pointed ends when critical Ca_E is exceeded. We found that, when Ca_E is below critical threshold, contrary to Oldroyd-B drops, the deformation of an LPTT drop shows non-monotonic behavior with De , it increases with De initially followed by a decrease with increasing De . Specifically, both $De = 0$ (Newtonian behavior) and very high De values result in pointed shapes at lower Ca_E . In contrast, intermediate De values require a comparatively higher Ca_E to induce pointed shapes, implying that the critical Ca_E first increases with De before subsequently decreasing. This indicates that in the PR_B^+ region, for intermediate De , increased viscoelasticity provides greater resistance to deformation, while for sufficiently large De , this resistance diminishes, and deformation is enhanced compared to a Newtonian drop. Overall, LPTT drops exhibit larger deformation compared to Oldroyd-B drops for all non-zero De values, indicating a lesser resistance to deformation as compared to Oldroyd-B drop.

For (σ_r, ϵ_r) from the OB^- region, an LPTT drop deforms into a stable oblate spheroidal shape below the critical Ca_E and drop breaks up above it. In stark contrast to Oldroyd-B drops, LPTT drops exhibit a non-monotonic relationship with De , where magnitude of deformation initially increases before subsequently decreasing, ultimately leading to the lower deformation at higher De . This fundamental difference suggests that at elevated De values, Oldroyd-B drops experience enhanced

deformation and are more prone to breakup, while LPTT drops demonstrate greater resistance to deformation and tend to be more stable.

References

- Aggarwal, N., Sarkar, K., 2007. Deformation and breakup of a viscoelastic drop in a newtonian matrix under steady shear. *Journal of Fluid Mechanics* 584, 1–21.
- Aggarwal, N., Sarkar, K., 2008. Effects of matrix viscoelasticity on viscous and viscoelastic drop deformation in a shear flow. *Journal of Fluid Mechanics* 601, 63–84.
- Ajayi, O., 1978. A note on taylor’s electrohydrodynamic theory. *Proceedings of the Royal Society of London. A. Mathematical and Physical Sciences* 364, 499–507.
- Allan, R., Mason, S., 1962. Particle behaviour in shear and electric fields i. deformation and burst of fluid drops. *Proceedings of the Royal Society of London. Series A. Mathematical and Physical Sciences* 267, 45–61.
- Alvarado, V., Manrique, E., 2010. Enhanced oil recovery: an update review. *Energies* 3, 1529–1575.
- Alves, M., Oliveira, P., Pinho, F., 2021. Numerical methods for viscoelastic fluid flows. *Annual Review of Fluid Mechanics* 53, 509–541.
- Bangar, S.S., Tomar, G., 2026. On large deformations of oldroyd-b drops in a steady electric field. *arXiv preprint arXiv:2602.01891* .
- Basaran, O.A., Gao, H., Bhat, P.P., 2013. Nonstandard inkjets. *Annual Review of Fluid Mechanics* 45, 85–113.
- Bentenitis, N., Krause, S., 2005. Droplet deformation in dc electric fields: the extended leaky dielectric model. *Langmuir* 21, 6194–6209.
- Blanchard, D.C., 1963. The electrification of the atmosphere by particles from bubbles in the sea. *Progress in oceanography* 1, 73–202.
- Brosseau, Q., Vlahovska, P.M., 2017. Streaming from the equator of a drop in an external electric field. *Physical review letters* 119, 034501.
- Dalal, S., Tomar, G., Dutta, P., 2016. Numerical study of driven flows of shear thinning viscoelastic fluids in rectangular cavities. *Journal of Non-Newtonian Fluid Mechanics* 229, 59–78.
- Das, D., Saintillan, D., 2017. Electrohydrodynamics of viscous drops in strong electric fields: numerical simulations. *Journal of Fluid Mechanics* 829, 127–152.

- Das, S.K., Bangar, S.S., Dalal, A., Tomar, G., 2026. Effect of viscoelasticity on electrohydrodynamic drop deformation. *International Journal of Multiphase Flow* 197, 105633.
- Deshmukh, S.D., Thaokar, R.M., 2013. Deformation and breakup of a leaky dielectric drop in a quadrupole electric field. *Journal of Fluid Mechanics* 731, 713–733.
- Dubash, N., Mestel, A., 2007. Behaviour of a conducting drop in a highly viscous fluid subject to an electric field. *Journal of Fluid Mechanics* 581, 469–493.
- Eow, J.S., Ghadiri, M., 2002. Electrostatic enhancement of coalescence of water droplets in oil: a review of the technology. *Chemical Engineering Journal* 85, 357–368.
- Esmaeeli, A., Behjatian, A., 2020. Transient electrohydrodynamics of a liquid drop at finite reynolds numbers. *Journal of Fluid Mechanics* 893, A26.
- Esmaeeli, A., Sharifi, P., 2011. Transient electrohydrodynamics of a liquid drop. *Physical Review E—Statistical, Nonlinear, and Soft Matter Physics* 84, 036308.
- Fattal, R., Kupferman, R., 2004. Constitutive laws for the matrix-logarithm of the conformation tensor. *Journal of Non-Newtonian Fluid Mechanics* 123, 281–285.
- Feng, J.Q., 1999. Electrohydrodynamic behaviour of a drop subjected to a steady uniform electric field at finite electric reynolds number. *Proceedings of the Royal Society of London. Series A: Mathematical, Physical and Engineering Sciences* 455, 2245–2269.
- Feng, J.Q., Scott, T.C., 1996. A computational analysis of electrohydrodynamics of a leaky dielectric drop in an electric field. *Journal of Fluid Mechanics* 311, 289–326.
- Ha, J.W., Yang, S.M., 1995. Effects of surfactant on the deformation and stability of a drop in a viscous fluid in an electric field. *Journal of colloid and interface science* 175, 369–385.
- Ha, J.W., Yang, S.M., 1999. Deformation and breakup of a second-order fluid droplet in an electric field. *Korean Journal of Chemical Engineering* 16, 585–594.
- Ha, J.W., Yang, S.M., 2000. Deformation and breakup of newtonian and non-newtonian conducting drops in an electric field. *Journal of Fluid Mechanics* 405, 131–156.
- He, H., Salipante, P.F., Vlahovska, P.M., 2013. Electrorotation of a viscous droplet in a uniform direct current electric field. *Physics of Fluids* 25.
- Hines, R., 1966. Electrostatic atomization and spray painting. *Journal of Applied Physics* 37, 2730–2736.

- Hooper, R.W., De Almeida, V.F., Macosko, C.W., Derby, J.J., 2001. Transient polymeric drop extension and retraction in uniaxial extensional flows. *Journal of non-newtonian fluid mechanics* 98, 141–168.
- Hua, J., Lim, L.K., Wang, C.H., 2008. Numerical simulation of deformation/motion of a drop suspended in viscous liquids under influence of steady electric fields. *Physics of Fluids* 20.
- Huh, H., Wirz, R.E., 2019. Numerical simulation of electrospray thruster extraction, in: *Proceedings of the 36th International Electric Propulsion Conference, Vienna, Austria*, pp. 15–20.
- Karp, J.R., Lecordier, B., Shadloo, M.S., 2024. Electrohydrodynamic flows inside a neutrally buoyant leaky dielectric drop. *Physics of Fluids* 36.
- Karyappa, R.B., Deshmukh, S.D., Thaokar, R.M., 2014. Breakup of a conducting drop in a uniform electric field. *Journal of fluid mechanics* 754, 550–589.
- Kelly, A., 1984. The electrostatic atomization of hydrocarbons. *J. Inst. Energy;(United Kingdom)* 57.
- Lac, E., Homsy, G., 2007. Axisymmetric deformation and stability of a viscous drop in a steady electric field. *Journal of Fluid Mechanics* 590, 239–264.
- Lanauze, J.A., Walker, L.M., Khair, A.S., 2013. The influence of inertia and charge relaxation on electrohydrodynamic drop deformation. *Physics of Fluids* 25.
- Lanauze, J.A., Walker, L.M., Khair, A.S., 2015. Nonlinear electrohydrodynamics of slightly deformed oblate drops. *Journal of Fluid Mechanics* 774, 245–266.
- Laser, D.J., Santiago, J.G., 2004. A review of micropumps. *Journal of micromechanics and microengineering* 14, R35.
- Lau, G.K., Shrestha, M., 2017. Ink-jet printing of micro-electro-mechanical systems (mems). *Micromachines* 8, 194.
- Law, S.E., 2018. Electrostatic atomization and spraying, in: *Handbook of electrostatic processes*. CRC Press, pp. 429–456.
- Lima, N., d’Avila, M., 2014. Numerical simulation of electrohydrodynamic flows of newtonian and viscoelastic droplets. *Journal of Non-Newtonian Fluid Mechanics* 213, 1–14.
- Liu, X., Chai, Z., Shi, B., 2019. A phase-field-based lattice boltzmann modeling of two-phase electro-hydrodynamic flows. *Physics of Fluids* 31.
- López-Herrera, J., Popinet, S., Herrada, M., 2011. A charge-conservative approach for simulating electrohydrodynamic two-phase flows using volume-of-fluid. *Journal of Computational Physics* 230, 1939–1955.

- López-Herrera, J.M., Popinet, S., Castrejón-Pita, A.A., 2019. An adaptive solver for viscoelastic incompressible two-phase problems applied to the study of the splashing of weakly viscoelastic droplets. *Journal of Non-Newtonian Fluid Mechanics* 264, 144–158.
- Melcher, J., Taylor, G., 1969. Electrohydrodynamics: a review of the role of interfacial shear stresses. *Annual review of fluid mechanics* 1, 111–146.
- Miksis, M.J., 1981. Shape of a drop in an electric field. *The Physics of Fluids* 24, 1967–1972.
- Moreau, E., Benard, N., Alicalapa, F., Douyère, A., 2015. Electrohydrodynamic force produced by a corona discharge between a wire active electrode and several cylinder electrodes—application to electric propulsion. *Journal of Electrostatics* 76, 194–200.
- Moriya, S., Adachi, K., Kotaka, T., 1986. Deformation of droplets suspended in viscous media in an electric field. 1. rate of deformation. *Langmuir* 2, 155–160.
- Nganguia, H., Young, Y.N., Layton, A., Hu, W.F., Lai, M.C., 2015. An immersed interface method for axisymmetric electrohydrodynamic simulations in stokes flow. *Communications in Computational Physics* 18, 429–449.
- Nganguia, H., Young, Y.N., Vlahovska, P.M., Blawdziewicz, J., Zhang, J., Lin, H., 2013. Equilibrium electro-deformation of a surfactant-laden viscous drop. *Physics of Fluids* 25.
- Nishiwaki, T., Adachi, K., Kotaka, T., 1988. Deformation of viscous droplets in an electric field: Poly (propylene oxide)/poly (dimethylsiloxane) systems. *Langmuir* 4, 170–175.
- O’Konski, C.T., Harris, F.E., 1957. Electric free energy and the deformation of droplets in electrically conducting systems. *The Journal of Physical Chemistry* 61, 1172–1174.
- O’Konski, C.T., Thacher Jr, H.C., 1953. The distortion of aerosol droplets by an electric field. *The Journal of Physical Chemistry* 57, 955–958.
- Paknemat, H., Pischevar, A., Pournaderi, P., 2012. Numerical simulation of drop deformations and breakup modes caused by direct current electric fields. *Physics of Fluids* 24.
- Phan, H.A., Nguyen, K., Pham, P.T., Do Quang, L., Thu, H.B., Lam, D.B., Jen, C.P., Thanh, T.B., Duc, T.C., 2025. On-demand electrostatic droplet sorting and splitting. *Sensors and Actuators A: Physical* 385, 116311.
- Popinet, S., 2015. A quadtree-adaptive multigrid solver for the serre–green–naghdi equations. *Journal of Computational Physics* 302, 336–358.

- Ramaswamy, S., Leal, L., 1999. The deformation of a viscoelastic drop subjected to steady uniaxial extensional flow of a newtonian fluid. *Journal of non-newtonian fluid mechanics* 85, 127–163.
- Saville, D., 1997. Electrohydrodynamics: the taylor-melcher leaky dielectric model. *Annual review of fluid mechanics* 29, 27–64.
- Sengupta, R., Walker, L.M., Khair, A.S., 2017. The role of surface charge convection in the electrohydrodynamics and breakup of prolate drops. *Journal of Fluid Mechanics* 833, 29–53.
- Sherwood, J., 1988. Breakup of fluid droplets in electric and magnetic fields. *Journal of Fluid Mechanics* 188, 133–146.
- Simpson, G., 1909. On the electricity of rain and its origin in thunderstorm. *Phil. Trans., A* 209, 397–413.
- Sozou, C., 1972. Electrohydrodynamics of a liquid drop: the time-dependent problem. *Proceedings of the Royal Society of London. A. Mathematical and Physical Sciences* 331, 263–272.
- Stone, H.A., Stroock, A.D., Ajdari, A., 2004. Engineering flows in small devices: microfluidics toward a lab-on-a-chip. *Annu. Rev. Fluid Mech.* 36, 381–411.
- Taylor, G.I., 1964. Disintegration of water drops in an electric field. *Proceedings of the Royal Society of London. Series A. Mathematical and Physical Sciences* 280, 383–397.
- Taylor, G.I., 1966. Studies in electrohydrodynamics. i. the circulation produced in a drop by an electric field. *Proceedings of the Royal Society of London. Series A. Mathematical and Physical Sciences* 291, 159–166.
- Tomar, G., Gerlach, D., Biswas, G., Alleborn, N., Sharma, A., Durst, F., Welch, S.W., Delgado, A., 2007. Two-phase electrohydrodynamic simulations using a volume-of-fluid approach. *Journal of Computational Physics* 227, 1267–1285.
- Torza, S., Cox, R., Mason, S., 1971. Electrohydrodynamic deformation and bursts of liquid drops. *Philosophical Transactions of the Royal Society of London. Series A, Mathematical and Physical Sciences* 269, 295–319.
- Vizika, O., Saville, D., 1992. The electrohydrodynamic deformation of drops suspended in liquids in steady and oscillatory electric fields. *Journal of fluid Mechanics* 239, 1–21.
- Vlahovska, P.M., 2016. Electrohydrodynamic instabilities of viscous drops. *Physical Review Fluids* 1, 060504.

- Vlahovska, P.M., 2019. Electrohydrodynamics of drops and vesicles. *Annual Review of Fluid Mechanics* 51, 305–330.
- Wagoner, B.W., Vlahovska, P.M., Harris, M.T., Basaran, O.A., 2021. Electrohydrodynamics of lenticular drops and equatorial streaming. *Journal of Fluid Mechanics* 925, A36.
- Wang, G., Lei, T., Yang, J., Fei, L., Chen, J., Luo, K.H., 2024. Lattice boltzmann modelling and study of droplet equatorial streaming in an electric field. *Journal of Fluid Mechanics* 988, A40.
- Wilson, C.T.R., 1921. Iii. investigations on lightning discharges and on the electric field of thunderstorms. *Philosophical Transactions of the Royal Society of London. Series A, Containing Papers of a Mathematical or Physical Character* 221, 73–115.
- Yariv, E., Frankel, I., 2016. Electrohydrodynamic rotation of drops at large electric reynolds numbers. *Journal of Fluid Mechanics* 788, R2.
- Zabarankin, M., 2013. A liquid spheroidal drop in a viscous incompressible fluid under a steady electric field. *Siam journal on applied mathematics* 73, 677–699.
- Zhang, J., Kwok, D.Y., 2005. A 2d lattice boltzmann study on electrohydrodynamic drop deformation with the leaky dielectric theory. *Journal of Computational Physics* 206, 150–161.
- Zhang, J., Zahn, J.D., Lin, H., 2013. Transient solution for droplet deformation under electric fields. *Physical Review E—Statistical, Nonlinear, and Soft Matter Physics* 87, 043008.
- Zhang, Y., Liu, Y., Ji, R., Wang, F., Cai, B., Li, H., 2011. Application of variable frequency technique on electrical dehydration of water-in-oil emulsion. *Colloids and Surfaces A: Physicochemical and Engineering Aspects* 386, 185–190.
- Zhao, J., Dzanic, V., Wang, Z., Sauret, E., 2025. Electrohydrodynamic effects on the viscoelastic droplet deformation in shear flows. *Physics of Fluids* 37.